Mercury Exosphere: I Global Circulation Model of its sodium component

François Leblanc, Robert E. Johnson

▶ To cite this version:

Accepted Manuscript

Mercury Exosphere: I Global Circulation Model of its sodium component

Francois Leblanc, R.E. Johnson

Please cite this article as: Leblanc, F., Johnson, R.E., Mercury Exosphere: I Global Circulation Model of its sodium component, *Icarus* (2010), doi: 10.1016/j.icarus.2010.04.020

Mercury Exosphere:
I Global Circulation Model of its sodium component

Francois Leblanc
LATMOS/IPSL, Université Versailles Saint Quentin, CNRS, France
francois.leblanc@latmos.ipsl.fr

and

R.E. Johnson
University of Virginia, Charlottesville, USA
rej@uva.edu

Abstract

Our understanding of Mercury's sodium exosphere has improved considerably in the last 5 years thanks to new observations (Schleicher et al. 2004) and to the publication of a summary of the large set of ground based observations (Potter et al. 2008; 2007; 2009). In particular, the non-uniformity in longitude of the dayside sodium distribution (the dawn/dusk asymmetry) has now been clearly observed. This suggests that Mercury's sodium exosphere is partly driven by a global day to night side migration of the volatiles. One of the key questions remaining is the nature of the prevailing sodium ejection mechanisms. Because of the uncertain parameters for each ejection mechanisms, solving this problem has been difficult as indicated by the numerous papers over the last 15 years with very different conclusions. In addition, the variation of the size and of the spatial distribution of the surface reservoir (Leblanc and Johnson, 2003) varies with distance from the sun affecting the importance of each ejection mechanism on Mercury's orbital position

We here present an updated version of the Leblanc and Johnson (2003) model. We take into account the two populations of sodium in the surface reservoir (Hunten et al. 1988), one ambient population (physisorbed in the regolith with low binding energy) and one source population (chemisorbed coming from grain interior or from fresh dust brought to the surface and characterized by a higher binding energy). We also incorporate a better description of the solar wind sputtering variation with solar conditions. The results of a large number of simulations of the sodium exosphere are compared with the measured annual cycle of Mercury sodium emission brightness. These measurements were obtained from the published data by Potter et al. (2007) as well as from our own data obtained during the last two years using THEMIS solar telescope. These data show that: the annual cycle in the emission brightness is roughly the same from one year to another; there are significant discrepancies

between what would be observed if the exospheric content were constant; and t the annual cycle of Mercury's sodium exosphere strongly depends on its position in its orbit so that there are seasons in Mercury's exosphere.

Based on these comparisons we derived the principal signatures for each ejection mechanism during a Mercury year and show that none of the ejection mechanisms dominates over the whole year. Rather, particular features of the annual cycle of the sodium intensity appear to be induced by one, temporarily dominant, ejection mechanism. Based on this analysis, we are able to roughly explain the annual cycle of Mercury's exospheric sodium emission brightness. We also derive a set of parameters defining those ejection mechanisms which best reproduce this cycle. For our best case, Mercury's exosphere content varies from $\sim 1.6 \pm 0.1 \times 10^{28}$ Na atoms at TAA=140° and 70° respectively to $\sim 4.5 \pm 0.3 \times 10^{28}$ Na atoms at TAA=180° and 0°. In addition, Mercury's exospheric surface reservoir contains $\sim 1 \times 10^{31}$ Na atoms at TAA=300° and at TAA=170° with up to three times more sodium atoms trapped in Mercury's nightside than in its dayside surface.

I **Introduction**

A dawn/ dusk asymmetry in the sodium emission from Mercury was first suggested by Hunten and Sprague (1997) using ground based observations and by analogy with the Moon's argon cycle (Hodges 1974). However, the presence of such an asymmetry in Mercury's sodium exosphere was debated for a long time because of a lack of clear observational evidence. As an example, Killen and Ip (1999) discussed this possibility, arguing that sodium atoms would not have time to migrate from day to night sides because of their short residence time in Mercury's exosphere as compared to argon in the lunar exosphere. However, Schleicher et al. (2004), observing the dependence of the exospheric sodium absorption feature on the solar flux during Mercury's transit of the Sun, demonstrated the existence of a strong asymmetry with a significantly denser exosphere at the dawn terminator than at the dusk terminator. This was later confirmed by Potter et al. (2006) when analyzing the large set of data they compiled over six years of regular observations of Mercury. They showed also that the dawn/dusk asymmetry varies in intensity during Mercury's year. Therefore, the analogy between Earth Moon's argon diurnal cycle and Mercury's sodium cycle might be relevant, but limited by the very different orbit of Mercury around the Sun. The analogy with the Moon's argon cycle only suggests that the sodium exosphere at Mercury can peak in density at the dawn because of the ejection of sodium in the early morning and because of the progressive depletion of Mercury's dayside surface with increasing local time.

The dawn/dusk asymmetry strongly suggests that the exospheric surface reservoir of sodium atoms available for ejection is finite and non-uniform in the local time. A uniform or infinite reservoir would result in an exosphere that peaked in an average around the subsolar longitude as it is the case for the Moon's sodium exosphere (Mendillo et al. 1995). Leblanc and Johnson (2003) (hereafter LJ2003) developed a model to describe the formation and

4

dynamic of Mercury's sodium exosphere during one annual cycle of Mercury. It was later used, along with a simple magnetospheric model (Delcourt et al. 2003), in order to dynamically couple the population of Na^+ with the neutral exosphere (Leblanc et al. 2003). In LJ2003, some of the possible exospheric signatures induced by the impoverishment of the dayside surface were Simulated. Killen et al. (2004) also calculated how surface depletion might impact the local surface ejection rates. These authors showed, as an example, how the reservoir for thermal desorption (TD) is quickly reduced with increasing local time, so that the TD rate becomes of the same order of magnitude as the photon stimulated desorption (PSD) rate (see Leblanc et al. 2007 for further explanations of these processes). These simulations and observations clearly suggest that the ejection rate of the sodium trapped in Mercury's exospheric surface layer decreases with increasing dayside local time because of depletion. This decrease would be negligible only if grain diffusion (induced by the surface charging as an example), gardening and other mechanisms brought new sodium atoms to the surface at a comparable rate. However, LJ2003 showed that, in that case, the exospheric brightness cannot fit the intensity observed from Earth (their Figure 12a). The typical range of observed Mercury's exospheric emission brightness allows us to determine the Na global ejection rate and, as a consequence, the intensity of the source flux of fresh sodium atoms from Mercury's surface. That is, the Na observations can be used to constrain the size and variation of the Na exospheric reservoir. Since the efficiency of any ejection process is controlled by the surface concentration of sodium, it will strongly depend on the efficiencies of all other ejection mechanisms that act to deplete this reservoir (Leblanc 2006).

Recently, Potter et al. (2006, 2007, 2008) analyzed six years of sodium Mercury's exosphere observations. These observations provide, for the first time, the sodium exospheric behaviour over Mercury's year and the opportunity to shed light on the anti-sunward transport of sodium

5

atoms induced by the solar radiation pressure (Potter et al. 2008). Thanks to these data and to our recent observations, we can now build a model of Mercury's sodium exosphere consistent with the annual cycle of Mercury's sodium exosphere. Since this model will describe the role of the global dayside to nightside circulation, we have called it Mercury Exosphere Global Circulation Model of its sodium component (MEGCMS). Since LJ2003, several changes have been made:

(a) The introduction of a source term equivalent to the amount of fresh sodium atoms brought to Mercury's exospheric surface layer by processes not yet specified. In the following, we will call the exospheric surface layer or reservoir, the top most surface layer from which sodium can be removed by one of the ejection processes into Mercury's exosphere. The magnitude of this source term is scaled to reproduce Mercury's annual cycle of the sodium emission brightness. By looking for a steady solution over a Mercury year this source rate is intrinsically coupled to our description of the loss rate.

(b) Four main processes of ejection (see section II.1) are included in a competitive way. That is, each process has its own efficiency to eject a sodium from the exospheric surface reservoir. Since, at any time the efficiency is small, ejection is dominated by the process with the highest efficiency. The main difference between LJ2003 and the present model is that we differentiate between the ambient and source populations of sodium atoms (Hunten et al. 1988). We use two binding energy distributions, one related to particles deeply bonded in the surface grains (the source atoms chemically bonded to the surface) and one in which the sodium is physisorbed, and hence more weakly bound to grains in the regolith, which we call the ambient population.

In this paper, we test our model by looking for a realistic set of parameters defining the ejection processes that lead to a good fit of Mercury's annual cycle of the sodium emission

6

brightness. First we briefly review the main properties of our model. We then describe the main characteristics of Mercury's annual exospheric cycle. The third and fourth sections are dedicated to comparisons between simulation and exospheric variations along Mercury's year. In the conclusion, we summarize what can be now established regarding Mercury's sodium exospheric origins and dynamics.

II MEGCMS

II-1-1 Model description

In order to describe the production of Mercury's sodium exosphere due to the various processes of ejection and the global motion of sodium induced by both gravity fields of Mercury and the Sun and by the solar radiation pressure, we use a Monte Carlo test-particle simulation. The motion of these particles is governed by the classical equation:

$$m\frac{d\vec{v}}{dt} = \vec{F}_M + \vec{F}_S + \vec{F}_{rad} + \vec{F}_{Cen} + \vec{F}_{Cor} \tag{1}$$

where m is the mass of the particle, t the time, $\vec{v}$ is the velocity vector of the particle in a reference frame attached to Mercury, $\vec{F}_M$ is the gravity acceleration due to Mercury, $\vec{F}_S$ is the gravity acceleration due to the Sun and $\vec{F}_{rad}$ is the acceleration due to the solar radiation pressure. $\vec{F}_{Cen}$ is the centrifugal force: $\vec{F}_{Cen} = -m\vec{\omega}_M \times (\vec{\omega}_M \times \vec{r})$ where $\vec{\omega}_M$ is Mercury diurnal rotation vector (taken perpendicularly to Mercury's orbital plane) and $\vec{r}$ is the position vector of the particle. $\vec{F}_{Cor}$ is the Coriolis force $\vec{F}_{Cor} = -2m\vec{\omega}_M \times \vec{v}$.

The ejected atoms are ultimately lost by ionization or escape from Mercury. Electron impact ionization is much less efficient than photon-ionization and is neglected. Therefore, the lifetime against ionization is equal to 1.9×10^5 s at 1 AU (Fulle et al. 2007). The boundaries of the simulation domain are Mercury's surface where particles can either be ejected or physisorbed and a sphere with a radius arbitrarily set equal to 50 R_M. At such a distance from

7

Mercury, the probability of a particle returning to the surface is negligible due to solar radiation pressure. This is smaller than the Hill radius of Mercury which varies from 70 R_M at perihelion to 105 R_M at aphelion. Solar radiation pressure is calculated with respect to heliocentric distance and radial velocity of each individual test-particle at any time step using the high resolution visible solar flux (Kurucz et al. 1984) for quiet Sun conditions and oscillator strengths that take into account all the solar resonant lines of Na listed in Morton (2003; 2004) as explained in Fulle et al. (2007). The surface accommodation and sticking probability for Na were assumed as described in LJ2003.

Mercury's exosphere is formed from several ejection processes (Leblanc et al. 2007). As in LJ2003, we considered the four processes thought to be the most important, namely thermal desorption (TD), photon stimulated desorption (PSD), solar wind sputtering (SWS) and micro-meteoroid vaporization (MMV). Magnetospheric Ion Sputtering (MIS) by returning Na^+ ions is also taken into account with the same characteristics used for SWS (Leblanc et al. 2003). Each process is defined by:

- an ejection efficiency: the probability for a sodium atom at a given position in the surface to be ejected by one of the above processes. This depends on the surface binding energy and is discussed for each process in section II.2.

- the energy distribution associated with each ejection process. We here used the same distributions as in LJ2003. Following Cassidy and Johnson (2005), these will be subsequently updated.

Unlike in LJ2003, we consider two populations of exospheric particles, one moving in Mercury's environment and one adsorbed on Mercury's surface as discussed. In addition, we do not describe Mercury's surface density on a given grid but keep track of the particles on

the surface. The approach and justification for this change are in section II.1.2. Because particle-particle collisions are not considered, for convenience the weight value of each test-particle may vary during the simulation. Such a variation is determined by our constraint to keep the number of exospheric and surface particles roughly constant during the whole simulation in order to limit the run duration. We typically use 1000 test-particles in the exosphere and 10^6 particles trapped in the surface. A run is stopped when the exospheric emission and total surface content do not vary by more than 1% from one Mercury year to another. Usually, 10 Mercury years are needed to reach a steady solution, which typically corresponds to few times 10^8 ejected particles and several weeks of run time on a computer cluster.

II-1-2 Source and ambient populations

In LJ2003, the trapped population was described by a surface density calculated on a defined grid. At each time step, a test-particle was numerically defined in each cell with a weight calculated from the surface density in this cell. A binding energy was also randomly chosen from a given distribution of possible binding energies (Yakshinskiy et al. 2000). The chosen binding energy is used to determine the probability of a test-particle being ejected by each of the four processes. The advantage of such a method was to avoid the description of a population of test-particle trapped in the surface. However, it can lead to an overestimate of the most efficient processes, as we will show in the following. By randomly choosing at each time step and in each cell a new binding energy from a given distribution in order to calculate the ejection probabilities, we did not separate the binding energies of the physisorbed and chemisorbed particles. With increasing resident time, a physisorbed Na can diffuse to a more tightly bonded site but slowly with respect to the simulation time step and temporarily at least on time scale equivalent to Mercury's day. Therefore, we have modified our model by

9

introducing a test-particle population trapped in the surface. Each time, an incident particle is physisorbed in the surface, a binding energy is randomly chosen for this test-particle from the distribution of binding energy deduced from laboratory's measurement for surface analogue of Mercury and the Moon (Yakshinskiy et al. 2000). Such binding energy is then fixed as long as this particle is not ejected from the surface. We therefore do not describe the evolution of the binding energy during the time a particle remained in the surface. Such an evolution may occur because of diffusion in the grain or in the regolith or because of change in the lattice of the grain surface induced by energetic particle bombardment or surface charging.

Smyth and Marconi (1995) were the first to describe the fate of sodium atoms ejected in Mercury's environment. They used the dual population of sodium atoms introduced by Hunten et al. (1988). The first population was named ambient and corresponds to atoms gravitationally bound to Mercury and moving stochastically around Mercury by subsequent hops. These particles are partially thermally accommodated to the local surface temperature and have counterparts absorbed in the regolith. A second population, named the source population, consists of sodium atoms released from the surface by energetic processes. They are non-thermal atoms that may either escape or become ambient particles after few impacts with the surface. These two populations coexist in the exospheric surface reservoir. Source atoms are chemically bonded to the grains with strong chemical bonds between the substrate and the absorbing atoms. These are predominantly ionically bonded to the oxygen in a bulk silicate (Madey et al. 1998) with a binding energy larger than 0.5 eV. Ambient atoms were assumed to be physisorbed with weak van der Waals forces and a binding energy less than 0.5 eV (Hunten et al. 1988). However, as shown by Madey et al. (1998), the difference between the ambient and source populations in the regolith is not as large as suggested by Hunten et al.

10

(1988), since the returning Na mostly reabsorbs in an ionic form with the binding energy determined by the local defect density.

Here, we also considered two binding energy distributions. The first one, corresponding to the ambient population, is the one measured by Yakshinskiy et al. (2000) which is consistent with sodium atoms reabsorbed in Mercury's regolith. This energy distribution was used in LJ2003 and is defined by a Gaussian distribution between 1.4 and 2.7 eV with a most probable value of 1.85 eV. This is significantly larger than the 0.5 eV suggested by Hunten et al. (1988) which was estimated on theoretical considerations rather than laboratory experiments. The second population was introduced in order to describe the source population of fresh atoms brought to the surface by meteoroid gardening or diffusion within grains. The binding energy distribution of this source population is chosen to be a Gaussian distribution between 2 and 3 eV and a most probable value of 2.5 eV (Madey et al. 1998; Killen et al. 2007). We also tested other distributions of energy (section IV.3).

II-1-3 Solar wind sputtering

Solar wind sputtering is an important process for populating the exosphere. It contributes to the observed sodium exosphere and its signature can be related to Mercury's magnetosphere interaction with the solar wind. Since LJ2003, several papers have explored the way the solar wind sputtering might vary with solar wind conditions. The role of the interplanetary magnetic field (IMF) in shaping Mercury's magnetosphere – solar wind interaction was described (Massetti et al. 2007) as well as the possible dependency of this interaction on Mercury's distance to the Sun (Sarantos et al. 2007). Moreover, Potter et al. (2006) analyzed the possible presence of high latitude peaks in Mercury's exosphere brightness and positively

correlated them with the average orientation of the IMF at Mercury's heliocentric distance in agreement with Sarantos et al. (2007) and Massetti et al. (2007).

Here, the IMF components are simulated in order to reproduce the typical sequence of variable IMF observed at Mercury. We then scaled the associated effective magnetospheric plasma impact area, its distribution between Northern and Southern hemispheres and its time variation in order to reproduce statistics in the analysis of Potter et al. (2006) and Sarantos et al. (2007). We started from a nominal bombarded surface: defined as being between 30° and 50° in latitude in the Southern and Northern hemispheres and between 70° and 110° in longitude. We use the same definition of longitude as in LJ2003 with 0° being the dawn terminator, 90° the subsolar longitude and 180° the dusk terminator. The area of this nominal surface is changed according to the given sequence of the IMF Bx, By and Bz components. In solar ecliptic coordinates, Bx is along the Sun-Mercury axis and is positive when away from the Sun, Bz is along the North-South axis of the rotational axis of Mercury (and is positive when pointing towards the North), and By completes the reference frame so that By is oriented from the dawn to dusk. We arbitrary set Bx to vary between -27 nT and 27 nT, By between -15 nT and 15 nT and Bz between 15 nT and -15 nT. These values are roughly in agreement with Sarantos et al. (2007). These authors analyzed Helios 2 data set at Mercury's heliocentric distance range and observed Bz component varying always between -10 and 10 nT with most probable value at 0 nT but with Bx component varying from -20 to 20 nT at aphelion and from -40 to 40 nT at perihelion with most probable value at ±15 and ±35 nT respectively. Massetti et al. (2007) and Sarantos et al. (2007) showed that the Bz component was opening Mercury's magnetosphere to solar wind penetration when negative and closing it when positive (by opened we mean that there exists reconnected magnetic field lines between solar wind and magnetosphere allowing the solar wind particles to reach the surface).

12

Following these authors, a dominant Bx component should also induce an opened magnetosphere, a positive Bx component inducing a preferentially Northern bombarded hemisphere (and vice versa). The By component should induce a shift in longitude of the bombarded region.

In this work, we mimic the role of the Bz and Bx component on Mercury's magnetosphere by randomly generating sequences of Bx, By and Bz components (see Figure 1, upper three panels). The length of each sequence was randomly chosen from a Gaussian distribution with most probable value equal to one hour. The magnitude of the size of the bombarded surface and of the North/South asymmetry was then scaled in order to follow Potter et al. (2006) analysis which stated:

- an averaged rate of ejection between Northern and Southern hemispheres that is equal,

- solar wind sputtering acts 45% of the time,

- between 16 and 28% of this time with a strong North / South asymmetry,

This scaling implies that the total sodium ejection rate is 25% of the rate if the nominal surface was permanently bombarded.

FIGURE 1

In Figure 1, the grey area represents a period of seven consecutive hours that mimics Mariner 10 flyby conditions of IMF in March 1974 (Figure 5 of Luhmann et al. 1998). The lowest panel of Figure 1 provides the total size of the bombarded surface in solid line (in percentage of the nominal surface) and in the Northern hemisphere only in dashed line. The IMF during the period simulated here was characterized by a positive period of Bx component, a

significantly negative By component and a variable Bz orientation. Positive Bz component corresponds in our model to a close magnetosphere. Massetti et al. (2007) emphasized that, even for positive Bz component, the surface of Mercury might be impacted when the Bx component is strong. In order to simplify our model in the absence of quantitative tools to introduce this condition, we followed Luhmann et al. (1998) and turned off the sputter source when Bz was positive. Moreover, we did not introduce a variation of the Bx component with respect to solar distance, and considered a Gaussian distribution for Bx centred on 0. Our nominal surface corresponds to 10% of the Northern hemisphere (or 5% of the dayside surface) which is in good agreement with the average effective open area calculated by Sarantos et al. (2007) at aphelion. However, Sarantos et al. (2007) suggested that the effective open area might be two times larger at perihelion than at aphelion because of the variation of the Bx component with Mercury's distance to the Sun. Therefore, we also consider a number of values for the effective open surface area. For simplicity we did not include a dependence of the size of the open area on either the dynamical pressure or on the size of the By component.

II-2 Ejection processes

Thermal desorption is traditionally defined by two parameters (Hunten et al. 1988), the binding energy and the vibrational frequency of a bound atom such that the rate of ejection of sodium atoms into the gas phase (in number of sodium atoms per second) is:

$$R_{TD} = \nu_{TD} \times C_{Na} \times \exp(-\frac{U}{k_B T_s}) \qquad (2)$$

where ν_{TD} is the vibrational frequency in the surface, U is the binding energy (or the desorption energy following Hunten et al. 1988), k_B is the Boltzmann constant, C_{Na} is the sodium concentration in the surface and T_s is the surface temperature. There was a typographic error in our definition of this rate in LJ2003 (Čapek and Borovička 2009). The

14

vibrational frequency is set to be equal to 10^{13} s^{-1} as in LJ2003 following Yakshinskiy et al. (2000) and Yates and Madey (1971). However, Killen et al. (2007), quoting Holmlid (2006), reported that such a value should be several orders of magnitude smaller. Therefore, in order to account for the uncertainties in the thermal desorption, we considered ν_{TD} between 10^9 and 10^{11} s^{-1}. TD was observed to shift to higher binding energy after prolonged 1 keV He$^+$ bombardment of a Na-covered SiO$_2$ surface (Yakshinskiy et al. 2000). This effect is not taken into account here but would decrease the efficiency of TD in particular regions of the surface and during particular portions of Mercury's orbit.

The rate of ejection by photon stimulated desorption R$_{PSD}$ (in number of sodium atoms per second) depends essentially on the flux of solar photons with energy larger than 5 eV impacting the surface and on a cross section:

$$R_{PSD} = Q_{PSD} \times c_{Na} \times F_{ph} \times \cos(\theta_{SZA}) \tag{3}$$

where Q$_{PSD}$ is the photon desorption cross section, F$_{ph}$ is the solar flux of photon with energy larger than 5 eV and θ_{SZA} is the solar zenith angle. Q$_{PSD}$ was chosen equal to 10^{-20} cm^2 in LJ2003 following Yakshinskiy and Madey (1999) laboratory measurements, but the effective value may vary with respect to the surface porosity (Cassidy and Johnson 2005). On the other hand, the solar flux F$_{ph}$ may vary strongly following the solar activity (Killen et al. 2001). Since we are discussing the average annual cycle of Mercury's exosphere, the possible short term variations induced by the solar activity will be not considered. Because of the uncertainties discussed above, the effective Q$_{PSD}$ is not very well constrained. Therefore, we will set Q$_{PSD}$ to values from 4×10^{-20} to 1×10^{-21} cm^2. PSD ejection efficiency may also strongly depend on the surface temperature (Yakshinskiy and Madey 2004). Yakshinskiy and Madey (2005) measured a decrease of the electron stimulated desorption (ESD) yield (which behaves in a similar way to PSD) by a factor 3 from 400 to 600 K surface temperature but the opposite

behaviour for the Na$^+$ PSD yield. The physics and chemistry of these dependences were not well understood.

For the third process of ejection, the solar wind sputtering, the rate of ejection is:

$$R_{SWS} = Y_{SWS} \times c_{Na} \times F_{SW} \qquad (4)$$

where Y_{SWS} is the yield that is the number of atoms ejected from the surface per incident solar wind particles. The yield is a measurement of the efficiency by which a solar wind ion ejects surface particles. In LJ2003, we set $Y_{SWS} = 0.06$ surface atoms/solar wind particles smaller than the value of 0.15 suggested by Killen et al. (2001) because we took into account the effect of the surface porosity. Cassidy and Johnson (2005) calculated that porosity effect should reduce the yield measured in laboratory on flat surface by a factor close to the factor 0.4 as suggested earlier by Johnson (1989). F_{SW} is the solar wind flux reaching Mercury's surface. As explained section II.1.3, F_{SW} is highly dependent on Mercury's magnetosphere interaction with the solar wind. In our approach, we arbitrarily set the nominal surface as corresponding to the typical surface area bombarded by solar wind at Mercury's aphelion. Sarantos et al. (2007) suggested that at perihelion such an area might be up to 2 times larger. Therefore, in order to explore the possible role of the solar wind we tested a range of Y_{SWS} values between 0.02 and 0.15 as well as varying the size of nominal surface area. SWS ejection efficiency may also strongly decrease with increasing surface temperature since SWS acts through both ion momentum transfer and ESD. Surface charging can be large at Mercury with surface potentials larger than 100 V by analogy with lunar observations, (Halekas et al. 2008), and, therefore, could also significantly impact the SWS efficiency. However, without better knowledge of this mechanism, we cannot specifically test its importance.

16

Unlike the three previous ejection processes, micro-meteoroid vaporization (MMV) is simply a gross ejection of a mass of material estimated from the literature. In LJ2003, this ejection rate was set equal to 5×10^{23} sodium atoms / s at perihelion (derived from Killen et al. 2001). This rate is only weakly dependent on the surface concentration since sodium is also contributed by the meteoroid material and is excavated from below the surface layer. Therefore, as in LJ2003, we assumed the MMV sodium contribution is independent of the surface content. Several recent works on the flux of incident micro-meteoritic grains impacting Mercury (Cremonese et al. 2005, Marchi et al. 2005, Borin et al. 2009) suggest a global vaporized contribution much larger than that inferred in LJ2003. Therefore, in the following, we will consider a range of possible ejection rate between $R_{MMV} = 5\times10^{23}$ and 5×10^{25} Na/s at perihelion.

II-3 Results

From the Monte Carlo model, we can derive snap shots of Mercury's exosphere and surface at any position of Mercury in its orbit. In order to calculate the spatial distribution of the column density and the corresponding emission brightness for any phase angle the radial heliocentric velocity of each test-particle must be accounted for as in LJ2003. This determines the efficiency of a particle to scatter solar photons (the g-factor) and is based on the same calculation as for the solar radiation pressure (see section II-1 and Fulle et al. 2007). We ignored the optical thickness of Mercury's exosphere which, therefore, leads to a slight overestimate of the emission brightness. However this difference should not be large since the maximum local optical thickness of the exosphere is typically smaller than one as estimated by Potter et al. (2007) from the D_2 and D_1 emission line intensities ratio. Potter et al. (2007) have also divided their data set between dawn and dusk side observations. In our model, we also calculated the emission brightness associated with each side of Mercury as seen from the

17

Earth with a phase angle of 90° (dawn side) or with a phase angle of +270° (dusk side). The phase angle is here defined as the angle between the Earth, the Sun and Mercury with from 0° to 180° view of Mercury's morning side and from 180° to 360° view of Mercury's evening side, 0° and 360° corresponding to the alignment of the Earth, Sun, Mercury (same convention as in Potter et al. 2007).

Before comparing simulated 2D images of the brightness with observation, the effect of the Earth atmospheric seeing is included. As explained by Sprague et al. (1997), seeing can be accounted for by convolving the simulated 2D emission brightness with a Gaussian distribution:

$$f(r) = f_0 \times \exp(-\frac{r^2}{\sigma^2}) \tag{5}$$

where r is the distance to the position where the emission brightness is being calculated, f_0 is a normalization factor, and σ is the one-sigma value of the seeing effect (the full width at half maximum, FWHM, being equal to $2 \times \sigma \times \sqrt{\ln 2}$).

FIGURE 2

Figure 2 displays an example of our simulation results. Panel a gives the 2D map of the simulated Na column density as it would be observed from Earth for a phase angle of 300° at a true anomaly angle of 110°. The values of the parameters defining each ejection mechanism discussed in section II-2 correspond to the nominal solution that is discussed in section IV-3 ($v_{TD} = 4 \times 10^{10}$ s^{-1}, $Q_{PSD} = 2.5 \times 10^{-20}$ cm² at TAA=110°, $Y_{SWS} = 0.075$, Surface$_{SWS}$= 10% of dayside surface, $R_{MNV} = 5 \times 10^{23}$ Na/s). Panel b gives the simulated exosphere density and the direction of the observations displayed in panel c. Panel c shows the observed brightness as

measured by THEMIS solar telescope on the 11/07/2008 with a spectral power resolution of 240,000 at the same TAA and phase angle (THEMIS, López Ariste et al. 2000, is a French-Italian solar telescope on the Canary Island of Tenerife with a 0.9 m primary mirror, with a central obscuration of 0.4 m, and a 15.04 m focal length). For comparison to this observation, in panels d, e and f three images of the Na D_2 emission brightness calculated from panel a are shown but for different values of seeing (FWHM): 0.87, 1.06 and 1.26 Mercury radius (R_M) (also given in arcsecond in Figure 2). Brightness calibration and calculation of the seeing value for THEMIS data are explained in Leblanc et al. (2008, 2009). The measured averaged seeing during this observation corresponds to panel e conditions with a dispersion due to variable atmospheric conditions covering a range of cases from panels d to f. Comparing e and c, it is seen that the simulated brightness emission spatial distribution and intensity are in good agreement with the observed emission brightness when taking into account atmospheric seeing.

Comparing panels a, d, e and f also provides an illustration of the effect of the atmospheric seeing on Mercury's exospheric emission. As suggested by Potter et al. (2006), the first effect is to move the peak of emission on the disk (see the peak at the limb in panel a, which is what would be seen from an Earth without atmosphere, and panels d from f with a peak clearly on the disk). Therefore, any ground based observation of a peak in emission brightness on Mercury's visible disk but close to the limb might be due to a peak in the column density at the limb, where the column density should obviously peak because of the path length through the exosphere. However, in our simulations, the brightness peak at the limb is due to release of the sodium atoms in the early morning. The maximum density in Mercury's exosphere is almost hidden by Mercury's disk during this observation, as indicated in panel b (the part of the exosphere seen by the observer corresponds to the part above the dashed line in panel b).

19

Indeed, we found a clear morning to evening asymmetry in the model with a ~5 times denser exosphere on the morning side than on the evening side (panel b).

Limb effects due to various path length through the exosphere may increase the apparent discrepancy between limb and subsolar regions but probably by not more than a factor 2, as can be deduced from panels a and b and as discussed by Potter et al. (2006). For this particular observation, we cannot rule out that a uniform exosphere might be roughly in agreement with THEMIS observations because of the uncertainty on the seeing effect. However, in any case, from mid morning (lower part of panels a, c and f in Figure 2) to the dawn terminator (upper part of panels a, c and f in Figure 2), the exosphere observed by THEMIS did not significantly peak in density, either at the subsolar point (which would have been the case for a uniform reservoir inducing a peak of the ejection rate of TD and PSD at the subsolar point), or at high latitude (due to SWS). This suggests there is a non-uniform reservoir in Mercury's surface as well as the absence, during that observation, of strong solar wind sputtering at high latitude.

III Mercury's exospheric annual cycle

Potter et al. (2006, 2007 and 2008) analyzed six years of ground based observations of Mercury's exospheric sodium D_2 emission line. These authors provided the first description of the annual variation of Mercury's exosphere using 102 days of observations covering the complete range of TAA and a large range of phase angle. In the following, their data set (Table 1 of Potter et al. 2007) is compared with model predictions and other observations. We will not use their calculated column density but the observed D_2 emission brightness (column 2 of their Table 1). Indeed, Potter et al. (2007) column density calculations assumed an average efficiency for sodium atoms to scatter solar photons highly dependent of the speed of

the atoms, hence, on the dominant ejection mechanism, on Mercury's exospheric dynamics and on Mercury's orbital position. In the same way, we did not consider their corrections due to phase angle, because here again it implicitly implies a property of Mercury's exosphere that we would like to evaluate.

In Potter et al. (2007), the emission brightness intensities are given per 1"×1" pixel in the field of view. However, since the meaning of 1" with respect to Mercury's size depends on the distance between Mercury and the Earth, we have multiplied all the values given by Potter et al. (2007) by the ratio of the angular size of one pixel over the angular size of Mercury during each observation. The data displayed Figure 3 are therefore the measured sodium D_2 line emission brightness intensities of Mercury's exosphere per area of Mercury's disk. The upper panel provides the cycle with respect to TAA whereas the lower panel provides the same cycle in Earth days.

We also plotted the 2007, 2008 and april 2009 of our own data set obtained using THEMIS solar telescope. The slit size was either 0.5"x118" (spectral resolution of 27 m Å) or 0.25" x 69.6" (spectral resolution of 15.9 mÅ). We used one camera to measure the D_2 at 5890 Å Na emission line. Details on the calibration and the extraction of the data and their uncertainty are described in Leblanc et al. (2008, 2009). During the first two years of the THEMIS campaign, we obtained complete scans of Mercury's Na exosphere for 43 days of observations. The Potter et al. (2007) data in Fig. 3 are derived from the average value of all the good quality images of Mercury's exosphere obtained during one day of observation. THEMIS data points correspond to the 213 scans made during the two years of observation. The main difference between these two sets of data is therefore, related to the exposure time used to obtain an image of Mercury's exosphere. It is typically around one hour in THEMIS observations for

one complete scan. In Potter et al. (2007), 30 to 45 seconds exposure time was used for each individual image. However, their data in Figure 3 correspond to an average of the best individual images obtained during each day of observation. Therefore, the exposure time of the Potter et al. data used in this paper might be much longer. Potter et al. data set described the variations of Mercury's sodium exosphere on an Earth day time scale whereas THEMIS data set described Mercury's sodium exosphere on a hour time scale and is therefore much more scattered. In both data sets, the same calibration approach was chosen, using Mercury's reflected light as a calibration lamp and calculating the theoretical measured reflected solar flux from Mallama et al. (2002) parameters.

As shown Figure 3, there is a rather good agreement between these two independent data sets. Only THEMIS measurements at a TAA around 270° seems to be significantly different from Potter et al. (2007) measurements. Such a difference can be due to the particular geometry of these observations. Indeed, these THEMIS observations were done with phase angle from 124° to 135° so that only a small part of Mercury's Na exosphere could be seen from Earth during these particular observations. The lower intensities may be due to the relatively small fraction of Mercury's exosphere seen from Earth and/or by the difficulty to derive a good intensity calibration using Hapke's model of reflectivity for such a large phase angle.

FIGURE 3

Figure 3 provides, therefore, a useful view of Mercury's annual cycle of Na emission brightness. Several features of this annual cycle are critical. The comparison between the observed emission intensity and the one that would have been produced by an exosphere containing the same amount of sodium during the whole cycle (dashed black line in the upper

panel) highlights that the exosphere content is far from being constant over a complete cycle. A constant total content in sodium atoms along one Mercury's year convolved with the photon scattering efficiency of these atoms (related to their Doppler shift and to their distance with respect to the Sun) induces two peaks in the emission at the maximum solar radiation pressure indicated by the two red vertical dashed lines in Figure 3. This then provides a baseline to which the actual observations are compared in order to understand the transients in the surface source rate.

The variations of Mercury's sodium emission brightness during the upleg (from 0° to 180° TAA, when Mercury is moving from its periapsis to its apoapsis) and downleg (from 180° to 360°) portions of Mercury's orbit are significantly different. It is mostly related to the difference in radiation pressure effect over Mercury's orbit resulting in the presence or not of an exospheric tail (Potter et al. 2008).

The two peaks in the emission brightness do not have similar intensities. When the dawn side of Mercury is observed (empty symbols), the downleg peak is ~15% brighter than the upleg peak for similar phase angles. When looking at the dusk side of Mercury (filled symbols), both peaks seem to have roughly the same intensity. The positions of these two peaks relative to 0° TAA are significantly different. The peak during the upleg part of the orbit is between 25° and 40° TAA, that is, between the end of the period of retrograde rotation of Mercury (at 25° TAA, this period being indicated by the gray area in Figure 3) and the maximum of solar radiation pressure (red vertical line). On the other hand, the peak during the downleg part of the orbit is at the position of maximum solar radiation pressure.

A second peak at TAA=100° is also apparent in the Potter et al. (2007) data set. This peak might be partly due to a localized increase in the dispersion of the measurements. However, there is a significant minimum at TAA~70° in both data sets. This is particularly surprising since a maximum in the brightness might be expected (dashed black line). This implies there

23

is a large decrease in the total exospheric sodium content along Mercury's orbit (section IV-3). At the end (25° TAA) and beginning (334° TAA) of the period of retrograde rotation of Mercury (grey areas in Figure 3), the increase in the brightness differs between downleg and upleg portions of Mercury's orbit. The brightness increases by a factor 4 to 5 from 25° and 40° TAA (that is in less than 5 Earth days, see lower panel) whereas nothing similar is observed between 319° and 334°.

Potter et al. (2006) also analyzed their data in term of dawn/dusk asymmetry concluding that dawn side exosphere is usually brighter than dusk side as can be seen in Figure 3. During most of Mercury's year, dawn and dusk asymmetries are small except for the period around 40° TAA where the dawn side emissions are significantly less bright than dusk side emissions. Due to the retrograde rotation of Mercury, the dawn side of Mercury between TAA=334° and 25° becomes a dusk side. Such a particularity was not taken into account when plotting Figure 3. However, the dusk side observations made around TAA=40° corresponded to particularly low phase angles meaning that a significant fraction of the dawn side was also observed. In that case, the average emission brightness, as plotted in Fig. 3, is not accurate enough to characterize differences between these two sides. The dawn/dusk asymmetry is much easier to observe at 90° phase angle, because in that case the dawn or dusk side is hidden by Mercury's disk. A brighter dawn side is apparent between 70° and 230° TAA, but the intensity is typically not much larger than ~25% of that from the dusk side. Potter et al. (2006) concluded that dawn enhancement was apparent from 0° to 140°, decreased to almost no enhancement between 140° and 240° , and finally increased again from 240° to 360°. This trend may be an artifact produced by differences in the phase angles and will need many more observations to be confirmed.

Figure 3 also suggests that the report by Potter et al. (1999) of a dramatic increase in the sodium emission brightness from 900 kR/Mercury area on November 13, 1997 (TAA=213°) to 3500 kR/Mercury area on November 20, 1997 (TAA=239) might be consistent with what is expected considering the details of an observation in Na D lines and not a transient effect. This increase appeared to be significant since the expected increase in emission brightness associated with a constant exospheric content is a factor 1.6 when taking into account only the variation of the g-factor (dashed black line, Figure 3). Using the annual cycle variation in Figure 3, the reported increase from TAA=213° to TAA=239°, is consistent with the normal increase of the emission brightness within this true anomaly angle range. This is the case since the increase of the scattering efficiency of the sodium atoms from 213° to 239° depends not only on the g-factor, that is, on Mercury's heliocentric distance and Doppler shift, but also on the solar radiation pressure (Potter et al. 2007). In our simulation for a constant exospheric content within this range of TAA, the emission brightness actually increases by more than a factor 2 from ~1400 kR/Mercury area to ~3400 kR/Mercury area. Therefore, there is rather good agreement between the apparent annual cycle and the reported measurements by Potter et al. (1999), except for the measurements on the first day, which is significantly weaker in intensity than the corresponding point on the annual cycle (Potter et al. 1999). Therefore, beside North/South variation of the emission peak position, the signal reported by Potter et al. (1999) may be a normal feature of Mercury's annual cycle. If confirmed by further observation within this range of TAA, this would rule out any significant enhancement due to coronal mass ejection (Potter et al. 1999), due to a significant change of both solar wind and solar flux conditions (Killen et al. 2001), due to an enhanced source in the Caloris basin (Sprague et al. 1990; Yan et al. 2006), or due to a shift of the bombarded surface by solar wind sputtering (Leblanc and Johnson 2003). Figure 3 suggests that the conjunction of variable IMF conditions with the increase in the scattering efficiency due to the increase of

Mercury's heliocentric velocity, and the variation of the solar radiation pressure may be able to produce the size of the observed increase in brightness.

IV Role of the main processes of ejection along an annual cycle

IV-1 Can the annual cycle of Mercury's exospheric emission brightness be related to one particular mechanism of ejection?

In the following, we describe the most important parameters constraining the annual cycle of the sodium exosphere. The first obvious parameter is the variation of the ejection efficiency of each mechanism with respect to Mercury's heliocentric distance, r:

- for TD, the ejection efficiency depends essentially on the surface temperature. Using equation (2) and Figure 1 of LJ2003, the TD ejection efficiency decreases by three orders of magnitude from perihelion (where the subsolar surface temperature is close to ~700 K) to aphelion (where the surface temperature at the subsolar is ~550 K),

- for PSD and SWS, the ejection efficiency depends on the solar photon and particle fluxes respectively, which vary as r^{-2} decreasing by a factor 2.3 from aphelion to perihelion. SWS may also change from perihelion to aphelion because of variable IMF conditions and solar dynamical pressure (Sarantos et al. 2007).

- the MMV ejection rate depends on the variation of the flux of micro-meteoroid impacting Mercury's surface and of their velocity. Killen et al. (2001) suggested a variation $\sim r^{-1.9}$ corresponding to a factor 2.2 decrease from aphelion to perihelion. Although, we used this, such a variation remains poorly constrained (see as an example Langevin et al. 1997) since it depends on the unknown contributions from the main asteroid belt and Sun grazing comets (Borin et al. 2009).

A second factor that may influence the annual cycle described Figure 3 are short time variations in the source rates. These can be neglected for TD and PSD when considering the

26

average annual emission intensity. This is the case even if there are significant variations during a solar cycle, a point that will be discussed in a forthcoming paper. As mentioned above, it may be important for the SWS ejection rate since short time variations of the solar wind flow and of the IMF can induce significant variations in the source rate (Leblanc et al. 2008). Since SWS is a highly variable source, we took it into account as described in section II.1.3. MMV may induce strong increase of the exospheric content when meter size impactor reaches Mercury (Mangano et al. 2005). However, such events are rare (one per Earth year, following Mangano et al. 2005) so that it should not influence significantly the global variation shown in Figure 3.

A third parameter that may have an important influence on the annual variation of the exospheric content is the energy distribution of the ejected sodium atoms. It determines the residence time of the sodium in Mercury's exosphere which in turn determines the time which a sodium atom spends in the exopshere. As an example, if 90% of the sodium in Mercury's surface are ejected by TD it does not imply that 90% of the sodium atoms present in Mercury's exosphere at a given time have been ejected by TD. The energy distribution of the ejecta also defines the ballistic distance trajectory and, therefore, defines the global loss and spatial redistribution rates. As an example, in the case of SWS, an ejected particle will reimpact the surface relatively far from its source so that the region of ejection is depleted in sodium atoms quicker than if the particles were ejected by a less energetic process. Therefore, as the dominant ejection process varies over the annual cycle, the map of the surface depletion can also vary significantly. This will be the case even if our knowledge of the energy distribution for each ejection process is only very rough. The most important aspect for the following discussion is that TD is the least energetic process and SWS is the most energetic and variable process (Figure 3 in LJ2003).

In Figure 4, we display the simulated average sodium D_2 emission brightness along Mercury's year for four different simulations. For each simulation, the efficiency of one of the ejection mechanism was changed in order for this mechanism to be significantly enhanced with respect to the other. By enhanced we mean that, during most of Mercury's year, either sodium atoms are ejected preferentially by such a process, which is the case for TD and PSD, or the percentage of particles present in the exosphere is significantly larger than that for the other ejection mechanisms, which is the case PSD, SWS and MMV and for TD at perihelion. In Figure 4, we chose $\nu_{TD} = 10^{11}$ s^{-1} for TD in panels a and e, $Q_{PSD} = 3\times10^{-20}$ cm^2 for PSD in panels b and f, Y_{SWS} =0.06 for SWS in panels c and g with the nominal surface bombarded 20% of Mercury's dayside North hemisphere (equivalent to Sarantos et al. 2007 for aphhelion conditions) and $R_{MMV} = 5\times10^{25}$ Na/s for MMV in panels d and h.

FIGURE 4

For each simulation, the supply rate is that rate at which fresh sodium atoms are brought to the exospheric surface reservoir by diffusion though a grain to its surface, gardening which can exposes fresh unirradiated grains and any other potential source process excluding the contribution brought to Mercury by MMV. The supply rate was fitted in order to provide the best global fit of the observations. Normalizing to the observations for the TD enhanced simulation, this supply rate at perihelion was found to be ~2.5×10^5 Na/cm²/s, for PSD ~1.6×10^6 Na/cm²/s, for SWS to 1.0×10^6 Na/cm²/s, and for MMV ~3.5×10^4 Na/cm²/s. As stated at the beginning of this paper, this rate plus the rate of new sodium atoms brought by MMV (equal to 1.4×10^6 Na/cm^2/s for TD, PSD and SWS enhanced simulations and to 1.4×10^8 Na/cm^2/s when MMV is enhanced) is, on average, equal to the loss rate over Mercury's year. The averaged supply rate is therefore equal to 1.5×10^6, 3.0×10^6, 2.4×10^6 and

1.4×10^8 Na/cm^2/s for TD, PSD, SWS and MMV enhanced simulations respectively. It is significantly smaller for TD enhanced simulation because fewer sodium atoms escape and is much larger in the case of MMV enhanced simulation which is a relatively energetic process of ejection (LJ2003). These rates can be also compared to the range of the average surface ejection rate which is between 10^7 and 10^8 Na/cm²/s for all the simulations.

As shown in Figure 4, although the general trend is reproduced, reflecting the sine-like variation in brightness, none of the simulations accurately fit the observed emission brightness intensity over a Mercury year. TD, PSD and SWS enhanced simulations produce two very different peaks in emissions, one being a few tens of percent brighter than the other one. Moreover, the positions of the two peaks do not match the observed ones at TAA=40° and TAA=300°. The simulation enhanced by PSD corresponds to an emission brightness intensity peaking at TAA= 110° and TAA=230° (Figure 4, panels b and f), for TD between 30° and 50° TAA and at TAA=300° (panels a and e), for SWS at TAA=50° and 290° (panels c and g) and for MMV at TAA = 60° and TAA=280° (panels d and h). Moreover, except for the MMV enhanced case, no simulation reproduces the two peaks with intensity as close to that observed.

When separated into the brightness observed on the dawn side of Mercury (left panels in Figure 4) and into dusk side emission brightness (right panels), the TD, SWS and MMV enhanced simulations are seen to be associated with dawn and dusk variations that are relatively close in magnitude. This is not the case for PSD between 150° and 350° where the dawn side simulated emission intensity is significantly stronger than the dusk side emission intensity.

FIGURE 5

29

In Figure 5, the annual variations of the total content of the exosphere (left panels) and of the surface (right panels) are displayed for the same four simulations. On average, there are between 100 to 1000 (TD, SWS and PSD enhanced simulations) to 10,000 (MMV enhanced simulation) times more particles in the exospheric surface reservoir of the ambient absorbed Na of Mercury than in its exosphere (Leblanc et al. 2007). The content of the surface is larger for TD and PSD than for SWS enhanced simulations, because more particles escape in the latter case. The surface content for the MMV enhanced simulation is much larger because the much larger total supply rate (dominated in that case by the MMV contribution) contributes significantly to the enrichment of the surface. For all the simulations, the total surface content peaks between TAA=110° and 160° and then decreases up to 300°. This variation is related to the inversed square of the distance dependence of the ejection and loss rates. It is also related to the terminator velocity where the release of particles from the surface is maximum. The downleg/upleg asymmetry is due to the solar radiation pressure which increases the global day to night side circulation during the upleg of Mercury's orbit and reduces it during the downleg. The dayside surface content represents 50% to 25% of the total surface content. It peaks at TAA=220° (downleg part) for TD, SWS and MMV dominated simulations and at TAA=200° for PSD dominated simulation. It is minimum at perihelion for TD, at TAA=40° for PSD and TAA=70° for SWS and MMV. There are, therefore, more particles available for ejection in the dayside surface during the downleg portion of Mercury's orbit than during the upleg portion.

The total content of the exosphere evolves in a very different way for each simulation as displayed in left panels in Figure 5. The results in the 4 panels are compared to each other in the following.

30

For the simulation in which TD is enhanced (panel a), the TD ejection rate produces the largest exospheric content from TAA=0° to 100° and from TAA=270° to 360°. The total content of Mercury's exosphere peaks exactly at the end of the retrograde rotation of Mercury at TAA=25° (dashed vertical line). Actually, the exosphere content increases when Mercury approaches the Sun from TAA=270° up to TAA=25°. The PSD enhanced case in panel b gives the largest exospheric content between TAA=100° and 270°. For SWS and MMV enhanced simulations in panels c and d, the exosphere content is almost constant from TAA=200° to TAA=25°, whereas it increases from TAA=340° to TAA=25° for the PSD enhanced simulation in panel b. The main difference between TD and the other mechanisms of ejection is the much lower energy of the ejecta when leaving the surface. The global migration efficiency is, therefore, smaller for TD, especially when the solar radiation pressure is very low, as it is the case at perihelion. As a consequence, the dayside surface is depleted slowly. Between TAA=340° and 25°, the terminator velocity is almost null so that the surface reservoir available for ejection into Mercury's exosphere remains slightly enriched due to transport by TD from regions close to the terminator as seen by the small enhancement in the surface dayside content at TAA=25° in Figure 5 panel e. As soon as TAA=25° is reached, the solar radiation pressure starts to increase significantly and quickly induces an increase in the loss rate, as well as an increase of the day to nightside migration. This change is most obvious for TD (panels a and e) because of the importance of the solar radiation pressure acceleration relative to the initial velocity of particles ejected by TD. Since other mechanism do not produce an enhancement in exospheric content at TAA=25° but only significantly later, it is probable that the observed peak in emission brightness between 25° and 40° is due, at least in part, to TD.

In the simulation in panels b and f in Figures 4 and 5, in which PSD is enhanced, a strong depletion of the dayside surface is seen at TAA=40° (close to the maximum of solar pressure).

At aphelion where the exospheric content peaks because the terminator velocity is maximum (LJ2003), the dayside surface total content peaks as well because the solar pressure is a minimum. The annual cycles of the exosphere and surface contents are seen to be related to the distance to the Sun, to the depletion of the dayside surface and to the velocity of the terminator. It is the variation of the exospheric content multiplied by the variation of the solar photon scattering efficiency which induces the two intensity peaks seen in Figure 4 panel b at TAA=110° and TAA=230°. These peaks are exactly at the same position as the secondary peaks at TAA=110° and a possible peak at TAA=230° in Figure 3. If confirmed by future observations, these two secondary peaks may be interpreted as a period during which PSD is dominant. In the same way, the minimum at TAA=70° in Figure 3 may be associated with the decrease of the PSD contribution to the exosphere as suggested by Figure 5 panel b. Indeed, near the perihelion, PSD is so efficient in depleting the dayside exospheric surface reservoir that a thick exosphere cannot be built. This is seen by comparing, in Figure 5, panel f to panels e, g and h dashed lines. Dawn/dusk asymmetry is also significant in the case of PSD as seen in Figure 4 panels b and f. This is the case because PSD dominates when the velocity of the terminator is maximum around Mercury's aphelion. In Figure 3, a clear dawn/dusk asymmetry is apparent between TAA=110° and 240° roughly where the PSD enhanced simulation predicts such an asymmetry and where Schleicher et al. (2004) observed it (at TAA=150°).

In the simulation during which the ejection rate of SWS was significantly increased (Figures 4 and 5 panels c and g), it is seen that the SWS dominates the other processes between TAA=150° and TAA=230°. In this simulation, the SWS ejecta dominate the exosphere except between TAA 80° and 100° when PSD and SWS contribute equally. In this example the global variation of Mercury's exosphere is smoother than for PSD because the exospheric content due to sputtering is less dependent on the terminator velocity. The minimum at TAA

= 100° (Figure 5 panel c) is due to the depletion of the region where solar wind sputtering preferentially occurs (high latitudes) favoured by the peak of solar radiation acceleration at TAA = 70° which reduces the proportion of sodium ejecta that reimpact this region. No similar minimum is observed on the downleg part of the orbit because the role of the solar radiation pressure is reversed so that day to night migration is less effective. The SWS enhanced simulations do not induce significant dawn/dusk asymmetry because the surface content of the solar wind impacted region is not affected by the velocity of the terminator.

The MMV enhanced simulation follows a pattern (Figure 5 panel d) similar to the SWS (Figure 5 panel c). Even though the MMV ejection rate is very large, it is seen not to be the dominant source populating the exosphere. This is the case since a large fraction of the sodium ejected by MMV is recycled and, because this process is also source of sodium for the surface. Therefore, the exospheric surface content is much larger than is the case for the TD, PSD and SWS enhanced simulations (Figure 5, panel h) increasing the rates for the other ejection mechanisms. In addition, no dawn/dusk asymmetry is apparent. In LJ2003 we introduced a leading (dawn side)/trailing asymmetry (dusk side) asymmetry of the impacting and ejected flux but did not see any related effect in the dawn/dusk exospheric distribution (LJ2003).

Further enhancing one of the ejection mechanisms with respect to the others would not improve the agreement with the observations. Therefore, the annual cycle of the emission brightness intensity displayed in Figure 3 cannot be due to an exosphere produced by a single dominant ejection mechanism but is, most probably, the product of a complex relation between these processes. As suggested by Figure 4, each of these processes is likely to be dominant for some specific part of Mercury's year. The position of the first peak of the sodium D_2 emission brightness intensity between TAA=25° and 40° is in a large part related

33

to TD. The position of the second peak at TAA=300° may be related to SWS, TD or/and MMV. The position of the putative secondary peaks at TAA=110° and 230° is likely induced by PSD. This conclusion contradicts that in LJ2003 on the dominant role of TD. This demonstrates the importance of improved simulations, in particular of the need to properly describe the trapped populations.

IV-2 A complex competitive situation

Because every ejection process affects the local surface content, each process is in "competition" with the others. Therefore, its efficiency for ejecting either the ambient or the source sodium will affect the other processes. As an example, in Figure 6, we show the effect of enhancing thermal desorption on the other processes. Two cases are displayed, one of which was already displayed in Figures 4 and 5 (panels a and e) and one in which the value of v_{TD} is changed. In these cases thermal desorption is the dominant from 0° to 80° and from 310° to 360°. The simulation using $v_{TD} = 10^{11}$ s^{-1} is shown in the middle panel in Figure 6 and the solid line in the upper panel. We also show a simulation in which the TD vibrational frequency was decreased to $v_{TD} = 10^9$ s^{-1} (dashed line in the upper panel). As seen in the middle panel, for the high TD efficiency, PSD and SWS compete between 100° and 280° with TD contributing around 10%. By contrast, in the lowest efficiency case given in the lower panel, the TD contribution to the exosphere never exceeds 10% and going as low as 1% around TAA=120°. In that case, PSD dominates with a significant contribution due to SWS around the aphelion.

By decreasing the efficiency of TD, the increase in the importance of the other mechanisms did not exhibit the same trends. In the part of the orbit that was dominated by TD, PSD significantly increased from TAA=0° to 140° and 150° to 360°. On the other hand SWS

34

increased only close to the perihelion where Mercury's surface is so hot that TD was efficient enough to also eject the population of chemisorbed sodium. This example also illustrates the importance of the distribution in the bond energies in the surface and the importance that the surface properties play in the origins of the exosphere. A decrease of the TD efficiency affects also the average loss rate which changes from 3.0×10^6 to 3.8×10^6 Na/cm²/s from $\nu_{TD} = 10^{11}$ s^{-1} to 10^9 s^{-1}.

FIGURE 6

In Figure 7 upper panel, the dashed line is from Figures 4 and 5 panels c and g where SWS is enhanced: 10% of the dayside surface and Ysw = 0.06. The separate source rates from this simulation are shown in the middle panel of Figure 7. This is compared to results from a simulation with SWS reduced: a nominal surface equal to 5% of the dayside surface (section II-1-3) and $Y_{SWS} = 0.02$ equivalent to a rate roughly 6 times smaller. These results are plotted in solid line (upper panel) with the individual contributions given in the lower panel of Figure 7. The upper panel of Figure 7 shows that in this second case the two peaks in emission occur with roughly the same brightness intensity in agreement with observations. In addition, the global scatter of the signal is much smaller, also in better agreement with observations than for the stronger SWS simulations. Here again, the relative contributions of each ejection process to Mercury's exosphere did not change independently. As an example, the percentage of particle ejected into Mercury's exosphere by MMV decreases by a factor 2 as seen by comparing the middle to lower panel when the efficiency of SWS was decreased.

FIGURE 7

35

IV-3 Origins of the annual cycle of Mercury's exospheric sodium emission brightness

We performed more than 90 independent simulations of Mercury's sodium exosphere with various values of the parameters for each ejection process in order to look for a solution providing a reasonable agreement with the Figure 3 data set.

FIGURE 8

We conclude that the annual variations of Mercury's sodium emission brightness cannot be reproduced by a set of constant parameters during a whole Mercury year. To illustrate this, we made two simulations with two sets of slightly different parameters. In one case the PSD cross section was made three times larger than in the other case: $Q_{PSD} = 1 \times 10^{-20}$ cm² (Figure 8) and $Q_{PSD} = 3 \times 10^{-20}$ cm² (Figure 9), with the other parameters set at $v_{TD} = 4 \times 10^{10}$ s^{-1}, Y_{SWS} = 0.075, Surface$_{SWS}$= 10% of dayside surface, $R_{MNV} = 7 \times 10^{23}$ Na/s. The supply rate of new atoms (excluding the contribution due to MMV) needed to reproduce the observations is equal to 8.5×10^5 Na/cm²/s in Figure 8 and 1.8×10^6 Na/cm²/s in Figure 9.

FIGURE 9

As seen in Figure 8, a simulation with a *small* cross section for the PSD can reproduce the two main peaks at TAA=30° and TAA=300°. It can also reproduce rather well the dawn and dusk cycles. However, it does not fit the secondary peak at TAA=100°. On the other hand, a simulation with a *large* PSD cross section reproduces correctly the local minimum in emission intensity at TAA=70° but displays several significant discrepancies with the observed emission during the rest of the orbit (Figure 9). Actually, as shown in Figure 4, the only process that can produce an increase of the emission intensity from TAA=70° to 110° is

36

PSD. This suggests that that the effective PSD cross section might not be constant over Mercury's orbit.

Such a prospect is also suggested by the laboratory experiments of Yakshinskiy and Madey (2004). They found that, depending on the type of sample, the PSD efficiency might increase by up to a factor 10 when increasing the temperature from 100 K to 470 K. This dependency was suggested to be due to the variation of the effective local bond energy of the trapped Na^+ with increasing temperature. Assuming this effect might occur in Mercury's surface material, we mimicked it by decreasing the supply of fresh Na to the exospheric surface reservoir with increasing heliocentric distance quicker than in the other simulations. That is, we carried out a simulation in which the supply rate was assumed to depend on the fourth power of the heliocentric distance rather than a power to the 1.9 used in the previous simulations. The main difference with the results shown in Figure 8, is a higher peak in intensity at TAA=30°, while the emission intensity after TAA=70° did not change at all.

Strong surface potentials have been recently reported at the Moon on the nightside (Halekas et al. 2008; 2009) and are likely at Mercury also. Since it is well established that charging affects the mobility of sodium in glas s(e.g., Miotello and Mazzoldi 1982), then depletion or enhancement can occur in the exospheric surface layer. On glasses if the surface is positively charged (typically of dayside surface if no large electron bombardment occurs), the sodium atoms diffused preferentially into the material. When the electron bombardment dominates the net balance at the surface (nightside regions as an example), negative charging of the surface occurs (as seen at the Moon, Halekas et al. 2009) inducing a significant diffusion of the Na atoms towards its surface. Therefore, electron and ion irradiation enhance the diffusion of the Na in the regolith due to the production of a non-uniform distribution of charge in the

material and defect production (Miotello and Mazzoldi 1984), processes suggested to be relevant at Mercury by McGrath et al. (1986). Possibly consistent with this, a recent set of observation of the Moon sodium exosphere (Wilson et al. 2006, Sarantos et al. 2008; 2009) suggest that plasma bombardment could increase the efficiency of PSD. They observed an increase in the sodium exosphere of the Moon after its passage through the Earth plasma sheet, where the plasma is denser and more energetic than in the rest of the magnetotail. This appeared to last at least 15 hours after the bombardment of the surface by plasma sheet particles. They suggested it was due to enhanced diffusion of the Na in the regolith due to plasma ion bombardment. As a matter of fact, negative surface charging in the shadow at the Moon surface was recently measured to be 2 to 10 times higher in the plasma sheet than in the plasma lobes of Earth magnetosphere (Halekas et al. 2008). Using all the available data on the Moon sodium exosphere, Sarantos et al. (2008; 2009) correlated the exospheric measurements with the available electron measurements at the Moon. They concluded that the PSD efficiency might increase by a factor of two for hours to even Earth days after a temporary, localized increase in the plasma flux. In our model, this change in the exospheric emission would be more related to a change in the content of the surface reservoir. Sarantos et al. (2009) suggested that this effect is equivalent to a change of the PSD efficiency because PSD is thought to dominate the Moon sodium production inside the Earth magnetosphere. At Mercury, both solar wind bombardment and surface charging should be stronger than at the Moon, especially at perihelion. Moreover, because of the length of Mercury's day, the role of the radiation-enhanced diffusion in the regolith might be significantly larger than at the Moon. That is, depletion of the exospheric surface reservoir is much more efficient at Mercury than at the Moon, so that any variation in the spatial distribution, nature and content of the sodium surface reservoir will have a much clearer signature in Mercury's sodium exosphere than in the Moon. At Mercury's perihelion, during more than 8 Earth days, the region of the surface

on the dayside is essentially the same, so that the regions close to the terminator but on the nightside also remain the same. Therefore, reabsorbed the exospheric ejected Na atoms accumulate during that period as described in our simulations. However, neither the effect of 8 Earth days of sporadic solar particles bombardment nor the effect of the potentially highly charged surface (Halekas et al. 2009) were simulated when describing the evolution of the exospheric surface reservoir close to the terminator. Since the lunar observations suggest that enhanced diffusion in grains induced by plasma sheet particle bombardment and/or surface charging might play a significant role in the formation of the Moon's sodium exosphere (Wilson et al. 2006; Sarantos et al. 2009), similarly at Mercury we might need to take into account changes in nature of the exospheric surface reservoir close to the terminator. This effect was recently suggested for the regions preferentially bombarded by the solar wind particles on the dayside (Mura et al. 2009).

The signature of such a change in the exosphere would occur when this surface reaches temperatures and solar zenith angle large enough to induce the sodium release. That would occur more than 10 Earth days after TAA=25°. Indeed, it takes ~20 Earth days for the terminator at perihelion, planetocentric longitude of ~90°, to move by 15° towards the subsolar point. Following our simulation displayed in Figure 2, panel b (realized at TAA=110°), 15° corresponds to the peak in release of the sodium atoms. Looking at this, in another way, it is only after ~20 Earth days that the perihelion terminator region reaches a local time where the surface temperature and photon solar flux are strong enough to eject efficiently the sodium atoms from the surface. As shown Figure 3 lower panel, 20 Earth days after the perihelion corresponds to the second peak of emission at TAA around 100°.

FIGURE 10

39

In order to evaluate the importance of the radiation-enhanced diffusion, we performed a few additional simulations. We changed the supply rate spatial distribution from a uniform one (as in all previous cases) to a day/night asymmetric distribution with from 70% to 90% of the newly source Na atoms created in the exospheric nightside surface reservoir. No significant change of the annual cycle derived from this simulation was produced showing that it is the recycled ambient Na population which dominates the Na atoms in this reservoir. We also performed simulation with different energy distributions for the source population. Distributions of binding energy for this population between 2.5 and 3.5 eV or from 1.5 to 2.5 eV were used in new simulations but no significant change in the annual cycle was produced, highlighting one more time that the ambient population is the main driver of the annual cycle.

The best agreement was found starting from the simulation displayed in Figure 8 in which we change the PSD cross section between TAA=70° and 160° in order to account for the change in the availability of weakly bound sodium in the surface ($v_{TD} = 4 \times 10^{10}$ s^{-1}, $Y_{SWS} = 0.075$, Surface$_{SWS}$= 10% of dayside surface, $R_{MMV} = 7 \times 10^{23}$ Na/s). In this interval, the PSD cross section was linearly increased by a factor 2.5 from TAA=70° and 100°, kept constant between 100° and 120° and linearly decreased by a factor 2.5 from TAA=120° to 160°. The simulated annual cycle of the sodium emission brightness is displayed Figure 10. The fit with the observation is considered to be good considering the large dispersion in phase angle of the data. Moreover, the peak around TAA=110° is also reproduced. The particularly large dispersion of the measurement at TAA=110° is not reproduced. This may be due to the origins of this peak for which solar wind impact is thought to be the major driver. The total flux of new atoms to the upper regions of Mercury's surface needed to best reproduce the observations is equal to 9.5×10^5 Na/cm²/s averaged over an annual cycle.

Since neither a change of the supply rate, nor a change of the supply spatial distribution, nor a change of the binding energy of the source particles produce a change equivalent to Figure 10, such an apparent change of the PSD cross section is most probably due to a change in the population of Na atoms reabsorbed in the exospheric surface reservoir (induced by radiation or charging of the surface). As an example, a shift of the binding energy of the particles in the surface reservoir towards higher energy would lead to a decrease of the TD efficiency and therefore an increase of the role of PSD in ejecting particles, since PSD is the main other process of ejection at TAA~100°. We have, therefore, performed other simulations by changing the binding energy distribution of the reabsorbed particles during the whole orbit to see if such a change is indeed equivalent to an increase of the PSD cross section (as displayed in Figure 9). Up to now, we used a binding energy distribution for the reabsorbed particles with energy between 1.4 and 2.7 eV with a most probable energy at 1.85 eV. We shifted this energy distribution by 0.15 eV up to 0.4 eV producing annual cycle close to the one displayed in Figure 9.

FIGURE 11

In Figure 11, we display the role of each ejection mechanism in producing the result in Figure 10. From Figure 11, we can conclude that:

- between TAA = 0° and TAA=70° and TAA=290° and TAA=360°, the ejection rate of sodium atoms by TD is dominant whereas the ejection rate by PSD is dominant from TAA=70° up to TAA=290°,

- the composition of the exospheric population does not follow the same pattern: TD is the main source of exospheric sodium atoms between TAA=0° and TAA=50° and TAA=330°

41

and 360°, whereas PSD is the major source of atoms between TAA=50° and 160° and between TAA=240° and TAA=330°. The SW is the major source of sodium atoms at aphelion in this scenario.

FIGURE 12

In Figure 12, we display the annual variation of the total content of Mercury's sodium exosphere as well as the content of the exospheric surface reservoir based on the model in Figure 10. This is one possible model which roughly fits the observation of the global changes in Mercury's Na exospheric brightness. The exospheric total content is seen to peak at TAA=180°-200° and at TAA=340°-360° at a value of $\sim 4.5 \times 10^{28}$ Na and reaches a minimum at TAA=70° at a value of $\sim 1.9 \times 10^{28}$ Na and at TAA=140° at a value of $\sim 1.5 \times 10^{28}$ Na. It is interesting that this pattern is not correlated directly to the surface total content. It stays roughly constant at $\sim 1 \times 10^{31}$ Na. Rather, it is more closely correlated to the dayside exospheric surface reservoir content which reaches minimum at 50° TAA and a maximum at 200° TAA.

V Conclusion

The origins of Mercury's sodium exosphere have been debated for a long time (Hunten et al. 1988; Killen and Ip 1999; Leblanc et al. 2007). One of the main reasons for the lack of agreement was related to the very few ground based observations of the sodium emission brightness. No statistical meaningful sample was available until only very recently. Potter et al. (2006; 2007; 2008) have now published 6 years of observations of Mercury's exosphere providing for the first time a set of data large enough to allow a statistical analysis of Mercury's sodium exosphere. Thanks to this data set, the annual cycle of Mercury's sodium emission brightness has now been characterized and several important features made manifest

(Potter et al. 2007). We here added to this data set our own extensive observations of Mercury's sodium brightness (Leblanc et al. 2008; 2009) using THEMIS solar telescope. The comparison between the two data sets displayed in Figure 3 is very good and highlights, in particular, new features in the annual cycle that were not obvious in Potter et al. (2007) data set.

In order to understand the complex trends in the sodium emission, we also presented an update version of our model of Mercury's sodium exosphere (Leblanc and Johnson 2003; Leblanc et al. 2003). We included two surface components for sodium, the ambient and the source populations, suggested by Hunten et al. (1988) and used by Smyth and Marconi (1995). To facilitate this, each test particle in our Monte Carlo simulations is permanently followed even during the time it is trapped in the surface. Its binding energy to the surface, as part of the ambient surface source, is kept constant as long as it remains trapped contrary to the procedure in Leblanc and Johnson (2003). In the latter, the returning atoms were assumed to return to the binding energies associated with the source distribution. Based on the extensive laboratory experiments of Yakshinskiy and Madey (2000), this is a more accurate description of the physical/chemical state of the surface which affects the competition between ejection mechanisms. The solar wind sputtering flux is also improved in order to take into account the typical interplanetary magnetic field orientation at Mercury's orbit (Sarantos et al. 2007) as well as its relation with the size of the area on Mercury's surface that is open to ions and electron flux (Sarantos et al. 2007; Massetti et al. 2007; Potter et al. 2006). Beside these changes, the ejection mechanisms, namely thermal desorption, photon stimulated desorption, solar wind sputtering and micro-meteoroid vaporization, are described as in Leblanc and Johnson (2003).

More than ninety different simulations were carried out in which each ejection mechanism was altered according to the solar conditions. Each run was then compared to the observed annual cycle of Mercury's sodium exospheric emission brightness. This approach allowed us to derive the most important properties of each of these ejection mechanisms and to highlight their potential observable signatures during a Mercury year. We here show that none of the ejection mechanisms proposed dominates during a whole Mercury's year consistent with the lack of agreement between models focusing on one or two specific processes of ejection for so many Earth years. In addition, we distinguish difference between the dominant source rates from those that dominate the instantaneous populations of the exosphere, also a source of controversy. However, it is also shown that certain mechanism do dominate the exosphere during specific parts of Mercury's year.

Based on this extensive set of simulations, with emphasis on our 'best' simulation results in Fig.10, thermal desorption (TD) is seen in Figure 11 to be an important process which dominates the pass through Mercury's perihelion and induces the observed peak in emission brightness between TAA=25° and 40°. During that portion of Mercury's orbit, the surface ejection rate is largely dominated by TD, but the percentage of sodium ejected by this process is lower than ~50 %. During the rest of the orbit, thermal desorption is a minor process of ejection. The main process of ejection during the rest of Mercury's year is photon stimulated desorption (PSD). Its most obvious signatures are the apparent secondary peaks or plateau at TAA=110° and TAA=230°. These features are essentially due to the dominance of PSD from TAA=60° to TAA=250° convolved with the efficiency of the sodium atoms to scatter solar photons. Moreover, PSD is the most efficient process inducing dawn/dusk asymmetries (Potter et al. 2007) as seen in Figure 4 panels b and f. Solar wind sputtering (SWS), also an important mechanism, is able to induce short time variation (Leblanc et al. 2008; 2009). This

can explain the large dispersion of the measured emission brightness during some portions of the orbit. The mechanism having the least obvious signature in Mercury's sodium emission brightness annual cycle is micro-meteoroid vaporization. Its main effect is to enrich the exospheric surface reservoir and, therefore, to increase the ejection rate of the other processes.

There remain several possible sources of uncertainties that we did not consider in this paper. In particular, the energy distribution of the ejecta defines their residence time in the exosphere, and, hence, their contribution to the instantaneous exospheric population. A good analogue of the energy distribution of the SWS was measured in laboratory by Wiens et al. (1997) for Na_2SO_4 pressed-powder samples. Lammer et al. (2003) commonly used analytic formula and concluded that the energy distribution may display a much larger energetic tail than Weins et al. distribution. However, Lammer et al. (2003) energy distribution is not well adapted to Mercury's regolith environment, since the porosity of the surface decreases the energetic tail of the distribution (Cassidy and Johnson 2005). A more energetic distribution of the SWS ejecta would increase the importance of SWS with respect to PSD. But, the respective contribution of each mechanism would remain close to what is described in this paper, since the increase in residence time would not change the respective ejection efficiencies. The other possible sources of uncertainty are related to the dependency of each mechanism's efficiency on the surface temperature (in particular TD, PSD or SWS) as well as on the magnitude of the surface weathering. The effect would be difficult to take into account without further laboratory studies. The annual cycle, as studied here, highlights the potential effect of enhanced diffusion due to ion bombardment and surface charging on the exospheric surface reservoir, as also suggested for the Moon's sodium exosphere (Wilson et al. 2006; Sarantos et al. 2009). Enhanced diffusion should be even higher at Mercury than at the Moon due to enhanced solar wind bombardment and surface charging. By analogy with the Moon's

crossing through the Earth plasma sheet (Wilson et al. 2006), we found that after Mercury's perihelion, the observations appear to be consistent with the PSD efficiency increasing by a factor up to 2.5 to explain the exosphere between TAA=40° up to TAA=140°. Such an effect may be due to the role of the incident ions making atoms in the regolith mobile, as suggested by McGrath et al (1986) for Mercury but also because of negative surface charging (Miotello and Mazzoldi 1982) occurring essentially on the nightside. Actually, one of the puzzling issues regarding the presence of high latitude peaks of emission in Mercury's exosphere is their duration (Leblanc et al. 2008; Mura et al. 2009). Indeed, in our model, as soon as the solar wind particles impact the surface, the surface is rapidly depleted and it is, therefore, difficult to maintain a localized emission peak for a few hours. However, if particle bombardment and surface charging induce not only ejection but also diffusion in the grains and change in the energy distribution of the reabsorbed particles, the duration of the observed peak might be explained. Lunar observation suggested that the signature of this process might last from few Earth hours to few Earth days (Wilson et al. 2006).

In simulating the observed Na emission we find, not surprisingly, that the Na exospheric content is not constant during Mercury's orbit. It reaches a minimum of 1.5×10^{28} Na at TAA=140° and peaks at aphelion and perihelion around 4.5×10^{28} Na. On the other hand, the exospheric surface reservoir (that is the part of the surface in contact with the exosphere constituted by ambient atoms reabsorbed in the surface and physic and chemisorbed atoms that can be ejected) varies from a minimum at TAA=300° of 1.0×10^{31} Na to a maximum of 1.1×10^{31} Na at TAA=200°. Such asymmetry between upleg and downleg of Mercury's orbit is due to the variation in the global day to night side migration. It is induced by the solar radiation pressure which accelerates sodium particles during the upleg, increasing the day to night side migration, and globally slowing down the sodium particles during the downleg.

46

This asymmetry and the role of the day to night migration is obvious when looking at the variation of the dayside exospheric surface reservoir during Mercury's year. Therefore, it is the global circulation of the sodium atoms from the day side to the night side, induced by the solar radiation pressure along Mercury's year, which is the main driver for the total content Mercury's sodium exosphere and which generates what could be called seasons in Mercury's exosphere.

References

Borin P., Cremonese G., Marzari F., Bruno M. and S. Marchi, Statistical analysis of micrometeoroids flux on Mercury, Astronomy and Astrophysics, In press, 2009

Čapek D. and Borovička J., Quantitative model of the release of sodium from meteoroids in the vicinity of the Sun: application to Geminids, Icarus, In press, 2009.

Cassidy, T.A. and R.E. Johnson, Monte Carlo model of sputtering and other ejection processes within a regolith, Icarus 176, 499-507, 2005.

Cremonese, G., Bruno, M., Mangano V., Marchi S., Milillo A., Release of neutral sodium from the surface of Mercury induced by meteoroid impacts, Icarus, 177, 122-128, 2005.

Delcourt, D.C., Grimald, S., Leblanc, F., Bertherlier J.-J., Millilo, A., and A. Mura, A quantitative model of planetary Na^+ contribution to Mercury's magnetosphere, Ann. Geophysicae, 21, 1723-1736, 2003.

Doressoundiram A., F. Leblanc, C. Foellmi, G. Cremonese, F. Donati, and C. Veillet, Sodium/Potassium ratio at Mercury with CFHT/Espadons and NTT/EMMI observations: Analysis and comparison with model, *Icarus*, Submitted, 2009.

Fulle M., Leblanc F., Harrison R.A., Davis C.J., Eyles, C.J., Halain, J.P., Howard, R.A., Bockelée-Morvan D., Cremonese G., and T. Scarmato, Discovery of the atomic iron tail of comet McNaught by the Heliospheric Imager on STEREO, *Astrophysical Journal*, 661: L93–L96, 2007.

Halekas, J. S., G. T. Delory, R. P. Lin, T. J. Stubbs, and W. M. Farrell (2008), Lunar Prospector observations of the electrostatic potential of the lunar surface and its response to incident currents, J. Geophys. Res., 113, A09102, doi:10.1029/2008JA013194, 2008.

Halekas, J. S., G. T. Delory, R. P. Lin, T. J. Stubbs, and W. M. Farrell (2009), Lunar surface charging during solar energetic particle events: Measurement and prediction, J. Geophys. Res., 114, A05110, doi:10.1029/2009JA014113.

Holmlid L., The alkali metal atmospheres on the Moon and Mercury: Explaining the stable exospheres by heavy Rydberg Matter Clusters, Planet. Space Sci. 54, 101–112, 2006.

Hunten, D.M., T.M. Morgan and D.M. Shemansky, The Mercury atmosphere, p. 562-612 in MERCURY, eds. F. Vilas, C. Chapman, M. Matthews, U. of Arizona Press, Tucson, 1988.

Johnson, R.E., Sputtering of a planetary regolith lunar rocks and soil Lunar. Sci.Conf.5th, Lunar, Icarus, 78, 206-210, 1989.

Killen, R. M., and W-H. Ip, The surface-bounded atmospheres of Mercury and the Moon, Rev. Geophys., 37, 361-406, 1999.

Killen, R.M. and A.E. Potter, P. Reiff, M. Sarantos, B.V. Jackson, P. Hick, and B. Giles, Evidence for Space Weather at Mercury. J. Geophys. Res., 106, 20,509-20,525, 2001.

Killen, R.M, Sarantos M. Potter A.E., and P.H. Reiff, Source rates and ion recycling rates for Na and K in Mercury's atmosphere, Icarus, 1-19, 2004.

Killen and 10 colleagues, Processes that promote and deplete the exosphere of Mercury, Space Sci. Rev., 132, 433-509, doi: 10.10007/s11214-007-9232-0, 2007

Kurucz, I.F., Brault J. & Testerman, L. National Solar Observatory Atlas No. 1) NSO/Kitt Peak FTS data used here were produced by NSF/NOAO, 1984.

Langevin Y., The regolith of Mercury: present knowledge and implications for the Mercury orbiter mission, Planet. Space Sci., 45, 31-37, 1997.

Lammer, H., P. Wurz, M.R. Patel, R. Killen, C. Kolb, S. Massetti, S. Orsini, and A. Milillo, The variability of Mercury's exosphere by particle and radiation induced surface release processes, Icarus, 166/2, 238-247, 10.1016/j.icarus.2003.08.006, 2003.

Leblanc F., and Johnson R.E., Mercury's sodium exosphere, *Icarus*, 164, 261-281, 2003.

Leblanc F., Delcourt D. and Johnson R.E, Mercury's sodium exosphere: Magnetospheric ion recycling, JGR-Planets, 108, E12, 5136, doi: 10.1029/2003JE002151, 2003.

Leblanc F., Mercury Exosphere – Magnetosphere – Surface relations, Advances in Geosciences, World Scientific Publication, Editor A. Bhardwaj, Vol. 3, 2006.

Leblanc F., Chassefière E., Johnson R.E., Hunten D.M., Kallio E., Delcourt D.C, Killen, R.M., Luhmann J.G., Potter A.E., Jambon A., Cremonese G., Mendillo M., Yan N. and A.L. Sprague, Mercury's exosphere: origins and relations to its magnetosphere and surface, Planetary Space Science, 55 1069–1092, 2007.

Leblanc F., A. Doressoundiram, V. Mangano, A. Lopez-Ariste, C. Lemen, B. Gelly, C. Barbieri, G. Cremonese and N. Schneider, High latitude peaks in Mercury's sodium exosphere: Spectral signature using THEMIS Solar Telescope, *Geophys. Res. Lett.*, 35, L18204, doi:10.1029/2008GL035322, 2008.

Leblanc F., A. Doressoundiram, N. Schneider, S. Massetti, M. Wedlund, A. López Ariste, C. Barbieri, V. Mangano, and G. Cremonese, On the short Time variations of Mercury's Na exosphere when observed with high spectral resolution, Geophys. Res. Lett., In press, 2009.

López Ariste, A., Rayrole, J. and Semel, M. (2000) First results from THEMIS spectropolarimetric mode, Astron. Astrophys., 142, 137.

Luhmann, J.G., C.T. Russell, and N.A. Tsyganenko, Disturbances in Mercury's magnetosphere: Are Mariner 10 "substorms" simply driven?, J. Geophys Res., 103, 9113-9119, 1998.

Madey, T. E., B. V. Yakshinskiy, V.N. Ageev, and R.E. Johnson, Desorption of alkali atoms and ions from oxide surfaces: Relevance to origins of Na and K in atmospheres of Mercury and the Moon." J. Geophys. Res. 103(E3): 5873 - 5887, 1998.

Mallama A., Wang D. and R.A. Howard, Photometry of Mercury from SOHO/LASCO and Earth, The Phase Function from 2 to 170 (2002), Icarus, 155, 253–264.

Mangano, V., Mura A., Milillo A., Orsini S., Marchi S., Lammer H., and P. Wurz, Modeling the implusive meteoritic impact vaporization in the hermean exosphere, Mem. S.A. It. Suppl, 6, 128, 2005.

Marchi, S. Morbidelli, A., Cremonese G., Flux of meteoroid impacts on Mercury, A&A, 431, 1123-1127, 2005

Massetti S., S. Orsini, A. Milillo, and A. Mura, Modelling Mercury's magnetosphere and plasma entry through the dayside magnetopause, Planet. Space Sci., 55, 1557–1568, 2007.

Mendillo M. and J. Baumdardner, Constraints on the origin of the Moon's atmosphere from observations during a lunar eclipse, Nature, 377, 404-406, 1995.

Miotello A and P Mazzoldi, Numerical analysis of field-assisted sodium migration in electron-irradiated glasses, J. Phys. C: Solid State Phys., 15, 5615-5621, 1982.

Miotello A and P Mazzoldi Cooperative transport effects in electron-irradiated glasses, Phys Rev Lett 54, 1675-1678, 1984

Morton D.C., Atomic data for resonance absorption lines. III Wavelengths longward of the Lyman limit for the elements hydrogen to gallium. *ApJSuppl.Ser.* 149, 205–238, 2003.

Morton D.C., Erratum "Atomic data for resonance absorption lines. III Wavelengths longward of the Lyman limit for the elements hydrogen to gallium. *ApJ Suppl. Ser.* 149, 205–238 (2003)". *ApJ Suppl .Ser.* 151, 403–404, 2004.

Mura A., Wurz P., Lichtenegger H.I.M., Schleicher H., Lammer H., Delcourt D., Milillo A., Orsini S., Massetti S. and M. L. Khodachenko, The sodium exosphere of Mercury: comparison between observations during Mercury's transit and model results, Icarus, 200, 1-11, 2009.

Potter, A. E., Morgan T.H. and R. M. Killen, Rapid changes in the sodium exosphere of Mercury, Planetary and Space Science 47: 1441-1448, 1999.

Potter, A.E., Killen, R.M. and Sarantos, M., Spatial distribution of sodium on Mercury, Icarus 181, 1, 2006.

Potter, A. E.; Killen, R. M.; Morgan, T. H., Solar radiation acceleration effects on Mercury sodium. Icarus, 186, 571-580, 2007.

Potter, A.E. and R.M. Killen, Observations of the sodium tail of Mercury, Icarus, 194, 1-12, 2008

Sarantos M., Killen, R.M. and K. Danheum, Predicting the long-term solar wind ion sputtering source at Mercury, Icarus, 55, 1584-1595, 2007

Sarantos, M., Killen, R.M., Sharma, A.S., Slavin, J.A., Influence of plasma ions on source rates for the lunar exosphere during passage through the Earth's magnetosphere, Geophys. Res. Lett. 35, L04105, doi: 10.1029/2007GL032310, 2008.

Sarantos, M., Killen, R.M., Sharma, A.S., Slavin, Sources of sodium in the lunar exosphere: Modeling using ground based observations of sodium emission and spacecraft data of the plasma, Icarus, In press, 2009.

Schleicher H., Wiedemann G., Wöhl H., Berkefeld T., and D. Soltau, Detection of neutral sodium above Mercury during the transit on 2003 May 7, A&A, 425, 1119–1124, 2004.

Smyth, W.H. and M.L. Marconi, Theoretical overview and modeling of the sodium and potassium atmospheres of Mercury, 441: 839-864, 1995.

Sprague, A. L., R. W. H. Kozlowski, and D.M. Hunten, Caloris Basin: An enhanced source for potassium in Mercury's atmosphere, Science 249 1140 - 1143, 1990.

Sprague, A. L., R. W. H. Kozlowski, D.M. Hunten, N.M. Schneider, D.L. Domingue, W.K. Wells, W. Schmitt, and U. Fink, Distribution and Abundance of Sodium in Mercury's Atmosphere, 1985 - 1988, Icarus 129: 506 - 527, 1997.

Wiens, R.C., Burnett, D.S., Calaway, W.F., Hansen, C.S., Lykkem, K.R., Pellin, M.L., 1997. Sputtering products of sodium sulfate: implications for Io's surface and for sodium bearing molecules in the Io torus. Icarus 128, 386–397.

Wilson, J.K., Mendillo, M., Spence, H.E., Magnetospheric influence on the Moon's exosphere, J. Geophys Res, 111 (A7), doi: 10.1029/2005JA011364, 2006.

Yakshinskiy, B.V., T.E. Madey and V.N. Ageev, Thermal desorption of sodium atoms from thin SiO$_2$ films, Surf. Rev. Let., 7, 75-87, 2000.

Yakshinskiy, B.V., and T.E. Madey, Photon-stimulated desorption of Na from a lunar sample: temperature dependent effects, Icarus, 168, 53-59, 2004.

Yakshinskiy, B.V., T.E. Madey and V.N. Ageev, Temperature-dependent DIET of alkalis from SiO$_2$ films: comparison with a lunar sample, Surf. Rev. Let., 593, 202-209, 2005.

Yan, N., Leblanc F. and E. Chassefière, Role of Caloris basin in producing short time variation of Na Mercury's exosphere, *Icarus*, 181, 348-362, 2006.

Yates J.T. and T.E. Madey, The absorption of Methane by Tungsten (100), Surf. Rev. Let., 28, 437-459, 1971

Figure 1: First three panels from the top: typical simulated sequence of variation of the IMF Bx, By, Bz (heliocentric coordinate frame). The gray part is a 7 hours sequence which can be compared with Figure 5 of Luhmann et al. (1998) showing Mariner 10 IMF measurement before and after its third flyby of Mercury. Bottom panel: corresponding simulated bombarded surface in nominal surface value (1.8×10^{16} cm² or ~5% of the dayside surface) in the North hemisphere (dashed line) and in the North+South hemispheres (solid line).

Figure 2: Example of comparison between our simulations (MEGCMS, panels a, b, d, e and f) and observation (THEMIS 11/07/2008, 11h00-12h00- UT, panel c). THEMIS observation was done with a slit of 0.5" placed along the North/South axis and moved along the East/West axis starting from the bottom part of the figure. Phase angle: 330°, TAA=108.7°, radial heliocentric velocity=9.53 km/s, elongation 10.95°, seeing was estimated as 1.06 R_M that is 2.69±0.31". The simulation was done using the best set of parameters described section IV-3. The seeing effect was taken into account following the approach described in the text. Panel a: column density calculated by MEGCMS (spatial resolution of the model) for the same position and phase angle than THEMIS observation. Panel b: Log10 of the density in Na/cm^3 in a band of ±10° centered on the equatorial plane (the white arrow indicates the view direction during THEMIS observation). Panels d, e and f: emission brightness intensity corresponding to panel a calculated for a seeing (FWHM) of 2.2", 2.7" and 3.2" respectively (same scale than panel c).

Figure 3: Measured emission brightness intensity in kilo-Rayleigh (kR) per Mercury's disk area plotted along an annual cycle with respect to True anomaly angle (Upper panel) and with respect to Earth day since Mercury's perihelion (Lower panel). Blue symbols are for Potter et al. (2007) data set treated as described in the text. The red symbols are for THEMIS Solar

telescope 2007-2008 campaigns. The size of the circles follows the sine of the phase angle (as indicated on each panel). Increasing size of the circle corresponds to increasing the observed proportion of Mercury's exosphere. Filled circles correspond to dusk side of Mercury (phase angle from 180° to 360°) whereas empty symbols to dawn side (phase angle from 0° to 180°). Vertical blue lines: perihelion and aphelion of Mercury. Vertical dark lines: reversal of the apparent motion of the Sun at Mercury. Vertical red lines: peak of solar radiation pressure and of solar photon scattering efficiency. Vertical green lines: peak of heliocentric radial velocity. The gray area highlights the period of Mercury's orbit during which dawn and dusk terminator are reversed. The dashed line in the upper panel is the emission intensity in the annual cycle that would have been produced by an exosphere with a constant content during the whole Mercury year.

Figure 4: Emission brightness intensity in kilo-Rayleigh (kR) per Mercury's disk area along an annual cycle (True anomaly angle) as simulated by MEGCMS (averaged over half an Earth day to mimic the Potter et al. 2007 observations). The simulated brightness is calculated for a phase angle of 90°. The size of the circle is the same as in Figure 3. Panels a and e: TD enhanced simulation ($v_{TD} = 10^{11}$ s^{-1}, $Q_{PSD} = 10^{-20}$ cm², $Y_{SWS} = 0.06$, Surface$_{SWS}$= 5% of dayside surface, $R_{MMV} = 5\times10^{23}$ Na/s). Panels b and f: PSD enhanced simulation ($v_{TD} = 10^{10}$ s^{-1}, $Q_{PSD} = 3\times10^{-20}$ cm², $Y_{SWS} = 0.06$, Surface$_{SWS}$= 5% of dayside surface, $R_{MV} = 5\times10^{23}$ Na/s). Panels c and g: SWS enhanced simulation ($v_{TD} = 10^{10}$ s^{-1}, $Q_{PSD} = 3\times10^{-21}$ cm², $Y_{SWS} = 0.06$, Surface$_{SWS}$= 10% of dayside surface, $R_{MNV} = 5\times10^{23}$ Na/s). Panels d and h: MMV enhanced simulation ($v_{TD} = 10^{10}$ s^{-1}, $Q_{PSD} = 5\times10^{-21}$ cm², $Y_{SWS} = 0.04$, Surface$_{SWS}$= 5% of dayside surface, $R_{MMV} = 5\times10^{25}$ Na/s). Left panels: dawn side emission. Right panels: dusk side emission.

Figure 5: Total number of Na atoms in Mercury's exosphere (right panel) and in Mercury's surface (left panel) as simulated by MEGCMS (averaged on half a day period). Rights panels: day+night sides (solid line), day side only (dashed line). Panels a and e: TD enhanced simulation ($v_{TD} = 10^{11}$ s^{-1}, $Q_{PSD} = 10^{-20}$ cm², $Y_{SWS} = 0.06$, Surface$_{SWS}$= 5% of dayside surface, $R_{MMV} = 5 \times 10^{23}$ Na/s). Panels b and f: PSD enhanced simulation ($v_{TD} = 10^{10}$ s^{-1}, $Q_{PSD} = 3 \times 10^{-20}$ cm², $Y_{SWS} = 0.06$, Surface$_{SWS}$= 5% of dayside surface, $R_{MMV} = 5 \times 10^{23}$ Na/s). Panels c and g: SWS enhanced simulation ($v_{TD} = 10^{10}$ s^{-1}, $Q_{PSD} = 3 \times 10^{-21}$ cm², $Y_{SWS} = 0.06$, Surface$_{SWS}$= 10% of dayside surface, $R_{MMV} = 5 \times 10^{23}$ Na/s). Panels d and h: MMV enhanced simulation ($v_{TD} = 10^{10}$ s^{-1}, $Q_{PSD} = 5 \times 10^{-21}$ cm², $Y_{SWS} = 0.04$, Surface$_{SWS}$= 5% of dayside surface, $R_{MMV} = 5 \times 10^{25}$ Na/s). The surface contents in panel h were divided by 30 to ease the presentation.

Figure 6: Upper panel: variation of the emission brightness intensity in kilo-Rayleigh (kR) per Mercury's disk area along an annual cycle (True anomaly angle) as simulated by MEGCMS (averaged on half a day period and for a phase angle of 90°) for $v_{TD} = 10^{11}$ s^{-1}, $Q_{PSD} = 10^{-20}$ cm², $Y_{SWS} = 0.06$, Surface$_{SWS}$= 5% of dayside surface, $R_{MMV} = 5 \times 10^{23}$ Na/s (solid line) and corresponding to the reduced TD case $v_{TD} = 10^{9}$ s^{-1} with other parameters fixed (dashed line in the upper panel). The size of the circle follows the same legend than in Figure 3. Only the dawn side emission is provided as well as the measured dawn emission intensities reported by Potter et al. (2007). Middle panel: percentage of the exospheric population produced by each of the processes corresponding to the dashed line of the upper panel. Lower panel: same than middle panel but in the case of the solid line of the upper panel.

Figure 7: Upper panel: variation of the emission brightness intensity in kilo-Rayleigh (kR) per Mercury's disk area along an annual cycle (True anomaly angle) as simulated by MEGCMS (averaged on half a day period and for a phase angle of 90°) for: $v_{TD} = 10^{10}$ s^{-1}, $Q_{PSD} = 3 \times 10^{-21}$

cm², Y_{SWS} = 0.02, Surface$_{SWS}$= 5% of dayside surface, R_{MNV} = 5×10^{23} Na/s (solid line) increasing SWS Y_{SWS} = 0.06, Surface$_{SWS}$= 10% of dayside surface, with other parameters fixed (dashed line). The size of the circle follows the same legend than in Figure 3. Only the dawn side emission is provided as well as the measured dawn emission brightness intensities reported by Potter et al. (2007). Middle panel: percentage of the exospheric population produced by each of the processes considered in this simulation (corresponding to the dashed line of the upper panel). Lower panel: same than middle panel (corresponding to the solid line of the upper panel).

Figure 8: Emission intensity in kilo-Rayleigh (kR) per Mercury's disk area along an annual cycle (True anomaly angle) as simulated by MEGCMS (averaged on half a day period and for a phase angle of 90°) in solid line for v_{TD} = 4×10^{10} s^{-1}, Q_{PSD} = 1×10^{-20} cm², Y_{SWS} = 0.075, Surface$_{SWS}$= 10% of dayside surface, R_{MMV} = 7×10^{23} Na/s. Upper panel: dawn side emission. Lower panel: dusk side emission. The circles represent the measured brightness as displayed in Figure 3 (same legend).
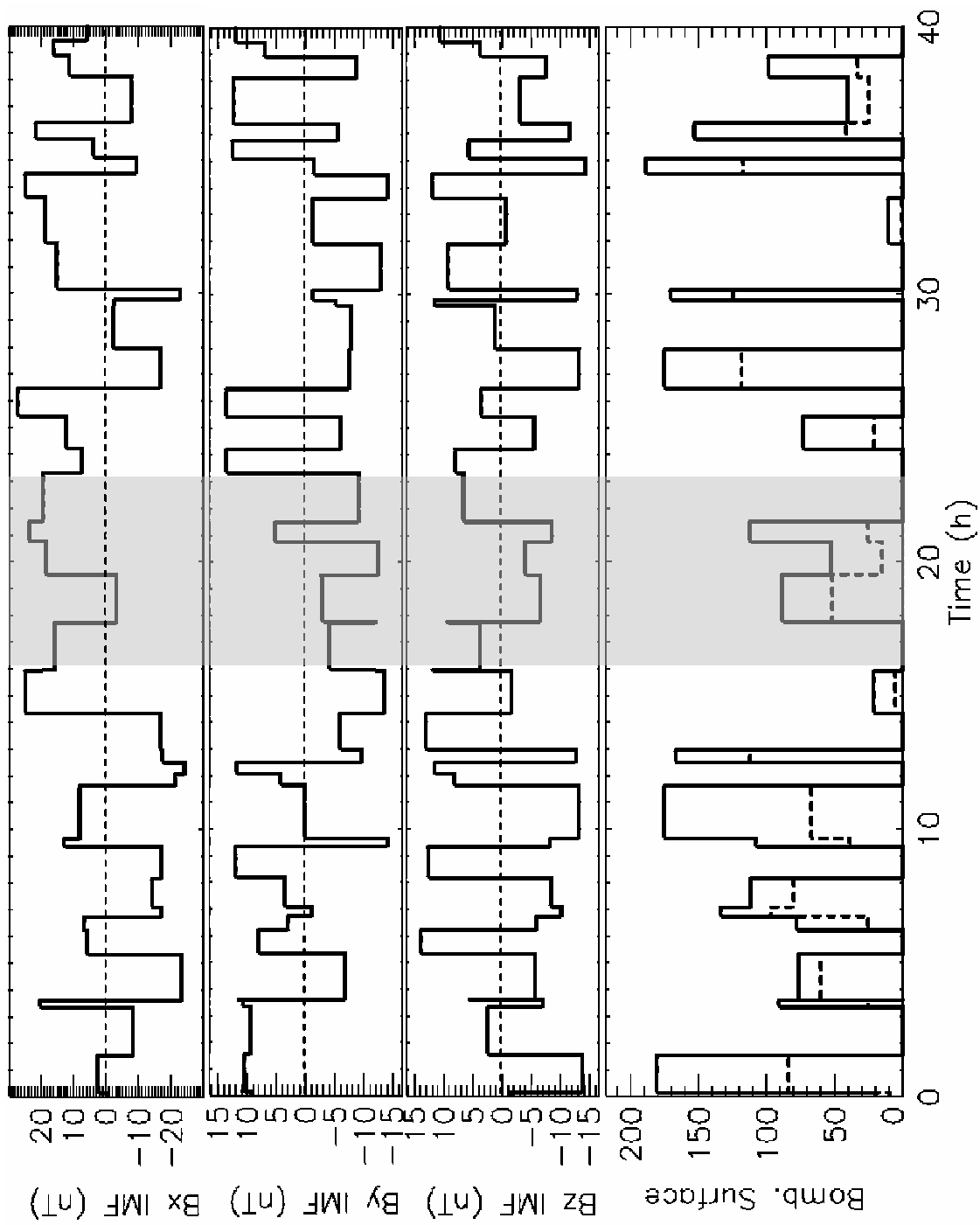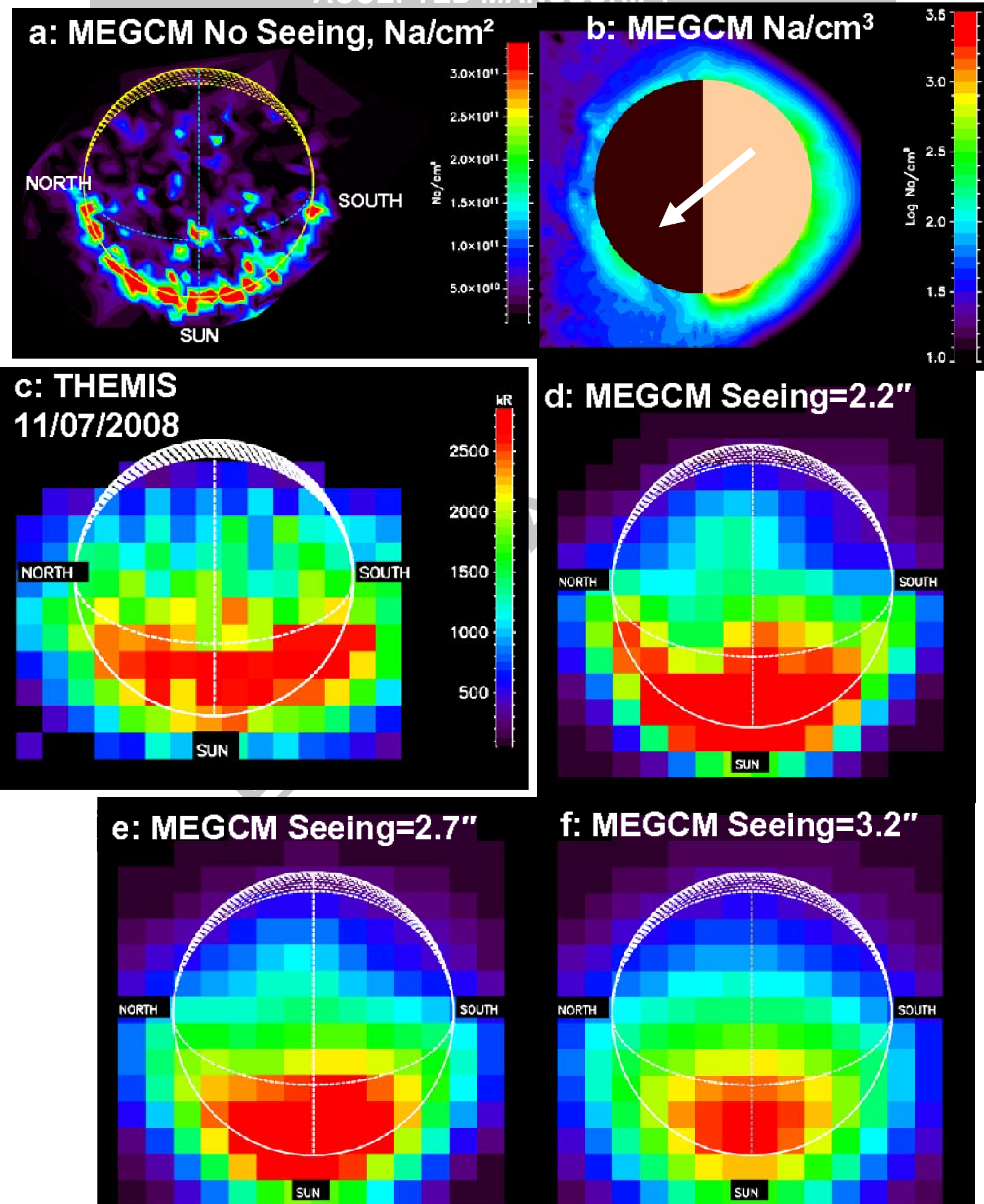
Figure 9: Emission intensity in kilo-Rayleigh (kR) per Mercury's disk area along an annual cycle (True anomaly angle) as simulated by MEGCMS (averaged on half a day period and for a phase angle of 90°): (solid line) for v_{TD} = 4×10^{10} s^{-1}, Q_{PSD} = 3×10^{-20} cm², Y_{SWS} = 0.075, Surface$_{SWS}$= 10% of dayside surface, R_{MMV} = 7×10^{23} Na/s. Upper panel: dawn side emission. Lower panel: dusk side emission. The circles represent the measured brightness as displayed in Figure 3 (same legend).

Figure 10: Emission intensity in kilo-Rayleigh (kR) per Mercury's disk area along an annual cycle (True anomaly angle) as simulated by MEGCMS (averaged on half a day period and for
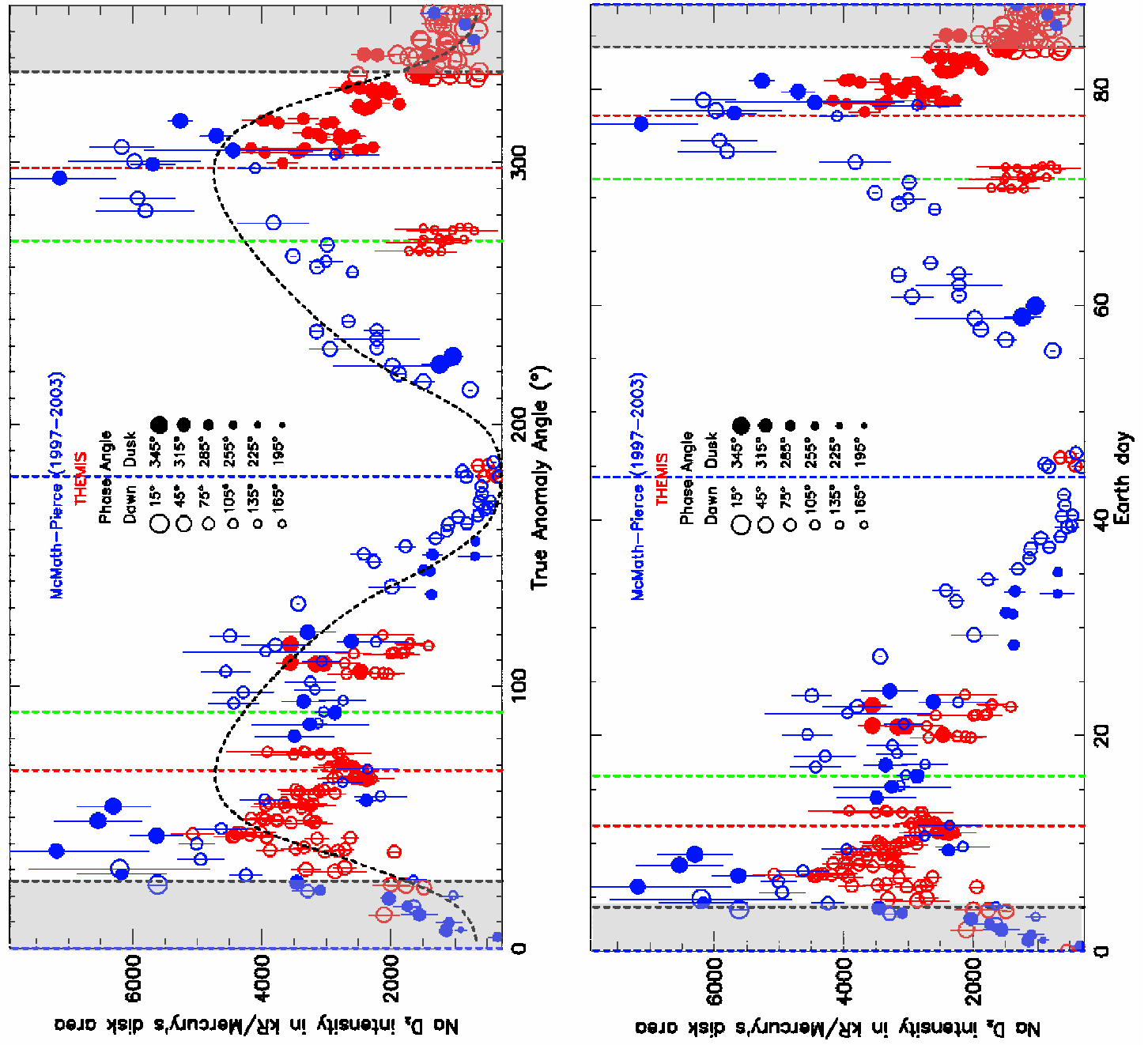
a phase angle of 90°): (solid line) for $\nu_{TD} = 4\times10^{10}$ s^{-1}, $Q_{PSD} = 1\times10^{-20}$ cm² except between TAA=70° and 160°. Within this interval, Q_{PSD} is linearly increased by a factor 2.5 from TAA=70° to 100°, then kept constant between 100 and 120° and decreases by a factor 2.5 from TAA=120° to 160°. $Y_{SWS} = 0.075$, Surface$_{SWS}$= 10% of dayside surface, $R_{MMV} = 7\times10^{23}$ Na/s. Upper panel: dawn side emission. Lower panel: dusk side emission. The circles represent the measured brightness as displayed in Figure 3 (same legend).
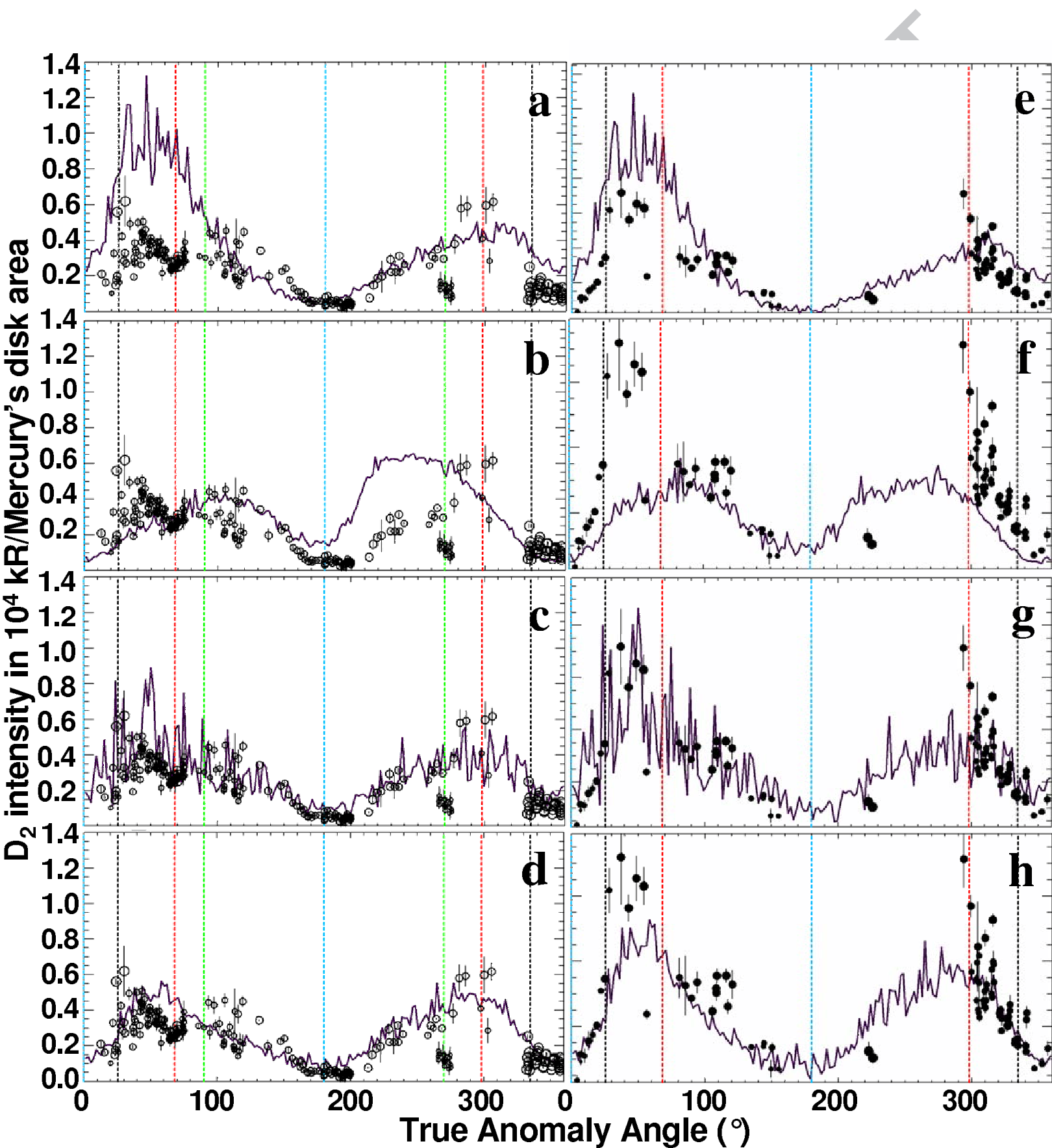
Figure 11: Lower panel: Percentage of the Na exospheric population produced by each of the processes considered in the simulation using the same parameters as in Figure 10. Upper panel: Na ejection rate for each processes of ejection.
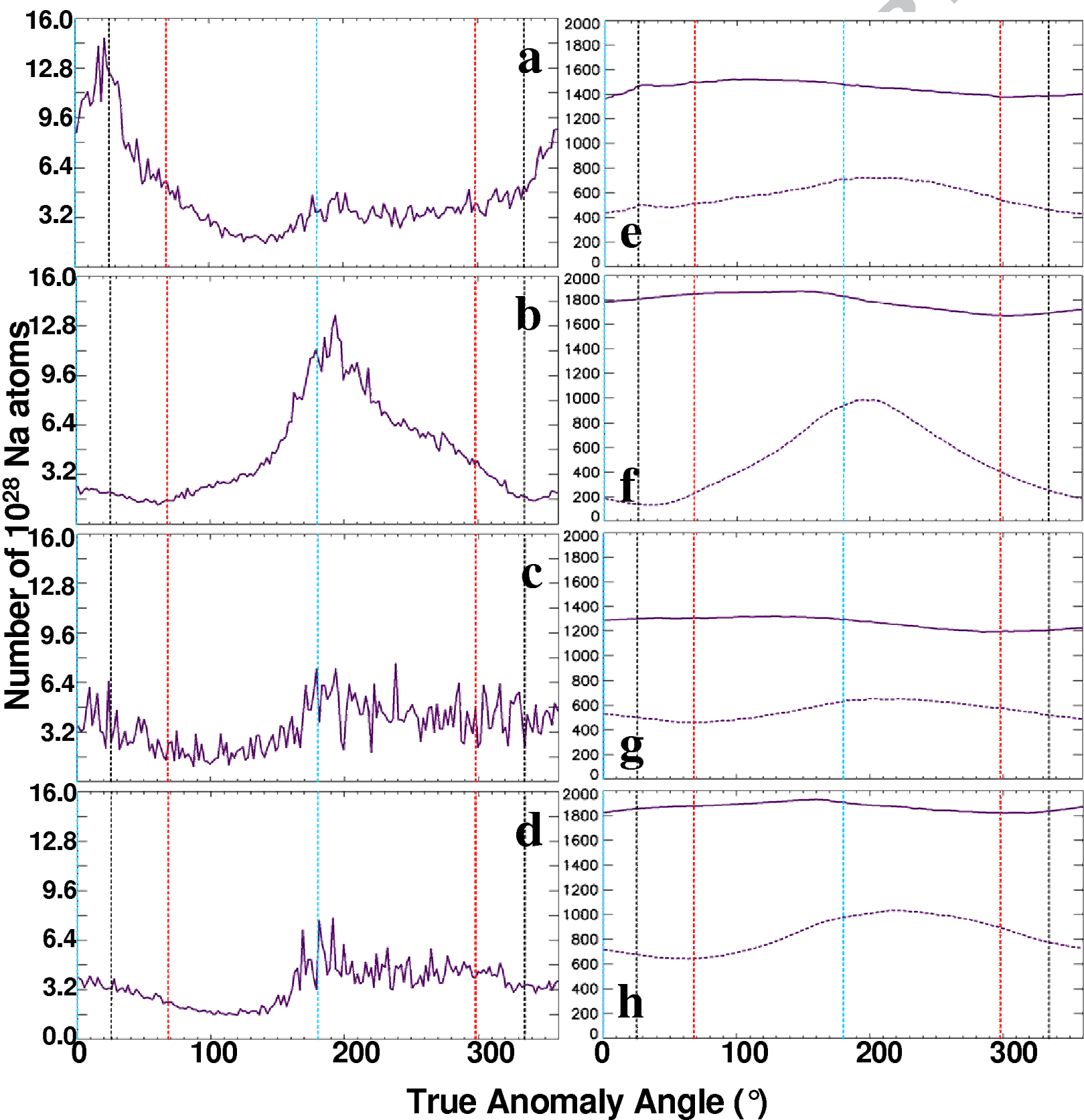
Figure 12: Upper panel: total number of Na atoms in the exosphere as obtained in the simulation using the same parameters as in Figure 10. Lower panel: total number of Na atoms in the surface (solid line) and in the day side surface (dashed line).
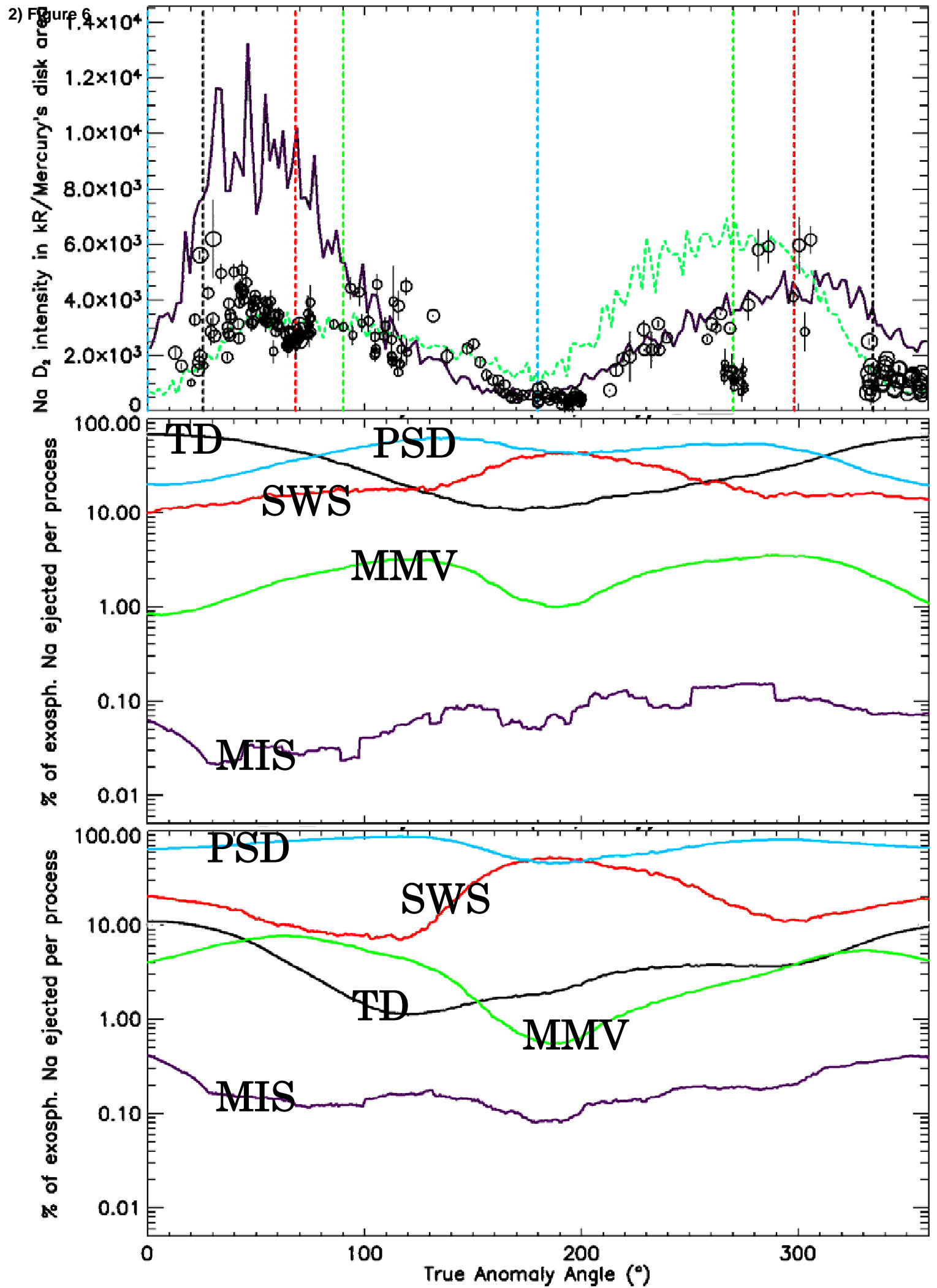
2) Figure 2

a: MEGCM No Seeing, Na/cm²

NORTH

SOUTH

SUN

b: MEGCM Na/cm³

c: THEMIS 11/07/2008

NORTH

SOUTH

SUN

kR

d: MEGCM Seeing=2.2″

NORTH

SOUTH

SUN

e: MEGCM Seeing=2.7″

NORTH

SOUTH

SUN

f: MEGCM Seeing=3.2″

NORTH

SOUTH

SUN

Na D$_2$ intensity in kR/Mercury's disk area

True Anomaly Angle (°)